Development of an Ultrasound-transparent Organ-on-chip Platform Towards Modeling Bubble-assisted Focused Ultrasound (BAFUS) Blood-brain-barrier (BBB) Disruption for Glioblastoma Therapy

by

Adam Rifat Akkad

A Thesis Presented in Partial Fulfilment
of the Requirements for the Degree
Master of Science

Approved April 2022 by the
Graduate Supervisor Committee:

Jian Gu, Co-Chair
Mehdi Nikkhah, Co-Chair
Marek Belohlavek
Xiao Wang

ARIZONA STATE UNIVERSITY

May 2022

ABSTRACT

The blood-brain-barrier (BBB) is a significant obstacle for treating glioblastomas and other neurological disorders. Bubble-assisted focused ultrasound (BAFUS) medicated BBB disruption is a promising technology that enables the delivery of large drug doses at targeted locations across the BBB. However, the current lack of an *in vitro* model of this process hinders the full understanding of BAFUS BBB disruption for better translation into clinics. In this thesis, a US-transparent organ-on-chip device has been fabricated that can be critical for the in vitro modeling of the BAFUS BBB disruption. The transparency of the device window to focused ultrasound (FUS) was calculated theoretically and demonstrated by experiments. The fluidic flow and drug diffusion within the device were modeled using finite element methods. Nanobubbles were fabricated, characterized by cryogenic transmission electron microscopy (cryo-TEM), and showed bubble cavitation under FUS. Human colorectal adenocarcinoma (Caco-2) cells were used to form a good cellular barrier for BAFUS barrier disruption, as suggested by the permeability and transepithelial electrical resistance (TEER) measurements. Finally, barrier disruption and recovery were observed in BAFUS disrupted US-transparent organ-on-chips with Caco-2 barriers, showing great promise of the platform for future modeling BAFUS BBB disruption *in vitro*.

ACKNOWLEDGEMENTS

I would like to acknowledge my primary mentor, Dr. Jian Gu, for all the support he afforded me throughout my graduate education and particularly for his contribution to advising me on this thesis manuscript. I would also like to thank all my thesis committee members including Dr. Mehdi Nikkhah, Dr. Marek Belohlavek, and Dr. Xiao Wang for their input and advisement on my project. I would like to thank Dr. Fredrich Zenhaeusern, the director of the Center for Applied NanoBioscience and Medicine (ANBM), for supporting me and the project financially and intellectually. I would also like to express my sincerest gratitude towards all the members of ANBM for supporting this project over the past two years. I give special thanks to Baiju Thomas for assisting with the design and production of 3D printed and machined components. I would also like to give special thanks to our undergraduate student, Missy Pear, for the assistance she provided in the nanobubble characterization and fabrication portion of this project. I would also like to give a great thanks to our collaborators at the Brain Tumor Unit of the Translational Genomics Research Institute, particularly Dr. Micheal Berens, Nanyun Tang, and Jayashree Iyer, for their intellectual support and for providing me with differentiated and cell line brain endothelial cells.

TABLE OF CONTENTS

Page

CHAPTER Page

LIST OF ABBREVIATIONS

Abbreviation	Meaning
BBB	Blood-Brain-Barrier
BBTB	Blood-Brain-Tumor-Barrier
BAFUS	Bubble Assited Focused Ultrasound
FUS	Focussed Ultrasound
US	Ultrasound
FFT	Fast Forier Transform
DIV	Dynamic *In Vitro*
B^3C	Blood-Brain-Barier Chip
TEER	Transepithelial Electrical Resistance
Caco-2	Human Colorectal Adenocarcinoma
HBECs	Human Brain Endothelial Cells
HBMECs	Human Brain Microvascular Endothelial Cells
iPSCs	Induced Pluripotent Stem Cells
PDMS	Polydimethylsiloxane
SLA	Stereolithography
PETE	Polyester Polytetrafluoroethylene
DPPA	1,2-Dipalmitoyl-sn-glycero-3-phosphate
DPPC	1,2-dipalmitoyl-sn-glycero-3-phosphocholine
DPPE	1,2-Dipalmitoyl-sn-glycero-3-phosphoethanolamine
DBPC	1,2-dibehenoyl-sn-glycero-3-phosphocholine

Abbreviation	Meaning
DSPE-mPEG	1,2-Distearoyl-sn-Glycero-3-Phosphoethanolamine-methoxyl-polyethylene glycol
TMR	Tetramethylrhodamine
LY	Lucifer Yellow
RT	Room Temperature
DI	Dionized
Cryo-TEM	Cryogenic Transmission Electron Microscopy

LIST OF TABLES

Table Page

LIST OF FIGURES

Figure Page

Figure Page

CHAPTER 1

INTRODUCTION

1.0 Overview

The blood-brain-barrier (BBB) is a protective, low permeability tissue structure that separates peripheral blood from the brain. It is composed of a myriad of supporting cells such as pericytes, astrocytes, and microglia. These supporting cells cause tight junctions to form between neighboring brain endothelial cells (1). Tight junction proteins, occludin and claudin, anchor themselves to the cytoskeletons of two adjacent endothelial cells. This produces a "tight" or leak-free seal between the cells in brain blood vessels. Blood vessels at other tissues/organs have less tight junctions between their endothelial cells with possible fenestration and transcytosis, which allows most molecules in the bloodstreams to move into surrounding tissues. Physiologically, the BBB protects the brain from exposure to toxins and pathogens that may be present in the blood. However, for delivery drugs targeted towards diseases of the brain, the BBB presents a major challenge.

The BBB prevents over 95% of drugs from entering the brain (2). Brain tumors such as glioblastomas exhibit altered BBB physiology called the blood-brain tumor barrier (BBTB). Drug permeability of BBTB in the bulk tumor regions is higher than a healthy BBB, which can help drug treatment of the tumor. However, the permeability of BBTB at the peripheral regions of the tumor is similar to a normal BBB, which turns out to still be a major barrier for brain tumor drug delivery (44). To address the drug delivery issue, multiple approaches have been taken to treat brain disorders such as brain tumors, dementia, Parkinson's disease and bipolar disorder, including viral vector, targeted

nanoparticle delivery, gene delivery via exosomes, drug permeability enhancers etc. (44). However, these approaches are still limited by lack of regional specificity, safety concerns, and the amount of drug that can be delivered.

Brain cancer affects 1% of people in the United States and it's the 10th leading cause of death (13). Glioblastomas are the most severe form of brain cancer with an estimated survival rate of less that 6% for individuals aged 55 or older (14). The need for new treatment methods for glioblastomas is pressing as standard chemotherapeutic medications do not have nearly as much success in the brain as they do in other parts of the body because of the BBB/BBTB. Usually, the best treatment option for patients with glioblastoma is to surgically remove the tumor and if that is not an option, the patient is left with radiation. Brain surgery and radiation are not trivial and can be accompanied by many complications. Sometimes removal of brain tumor and surrounding tissue can result in significant motor sensory deficits. Moreover, recovery from brain surgery can be lengthy and difficult. There is a significant demand for an additional technique to the current methods used to treat brain cancer.

1.1 Statement of the Problem

Clinical trials for a new treatment against glioblastoma using ultrasound (US) and microbubbles are currently underway based on promising pre-clinical data (3). The technique is described as bubble assisted focused ultrasound (BAFUS) BBB disruption. In other words, when micro/nanobubbles injected into the blood are stimulated by a FUS beam at low frequency (~ 1 MHz or lower for low scattering by the skull) near a glioblastoma, they cavitate to generate acoustic pressure and physically disrupt the BBB

to allow chemotherapeutic drugs to move into the tumor site (4). Studies showed the disruption can be temporary with BBB recovery observable 4-6 hours after BAFUS (5). It provides a promising way to deliver large dose of drugs across BBB at targeted locations.

Even though promising, some adverse effects (e.g. failed opening, microhemorrhage) were reported in early clinical trials. There is still a need to better understand the BAFUS BBB opening process to facilitate a safe and effective treatment, which is not fully understood at the cellular and molecular level yet. For example, in this precision medicine era, it is prudent to assume not everyone will respond BAFUS in the same way. It is therefore important to understand how the BAFUS parameters affect the BBB disruption and recovery at an individualized level.

To study the process in animals can be expensive. The results can also be misleading due to species differences. And it can be unethical to study the process in humans. The current lack of an in vitro model for BAFUS BBB disruption greatly hinders our understanding of the process. The focus of this thesis is to design an organ-on-chip platform that can be used to test how BBB disruption responds to the different BAFUS parameters. A BBB-on-Chip was created that is transparent to ultrasound, enabling accurate BAFUS power administration that has not been reported in the literature. Another advantage of this technology is its optical transparency that makes the BBB-on-Chip easy to image and monitor throughout culture.

1.2 Objectives and Organization

The long term objective of the project is to demonstrate that the BBB-on-Chip could be used to elucidate individual responses to BAFUS by testing human brain

microvascular endothelial cells (HBMECs) with varying tight junction alleles and genetic makeups. Genetic differences in tight junctions in human have been reported (6) and it is possible that genetics would influence how individuals respond to BAFUS. Therefore, a platform that enables testing of genetically different HBMECs would be very useful for determining the role of genetics in the success of this new treatment option for glioblastoma patients.

Currently, our collaborator at Translational Genomics Research Institute (TGen) is working on differentiating induced pluripotent stem cells (iPSCs) with different tight junction alleles into HBMECs. For the purpose of demonstrating an *in vitro* organ-on-chip platform, Caco-2 cells were chosen to study the BAFUS barrier disruption. Caco-2 cells have been observed to have good barrier properties with high trans-endothelial/epithelial electrical resistance (TEER) values, low permeability, and tight junction formation (7). Caco-2 cells are also easy to grow with short differentiation time to peak barrier properties after 24-72 hours of culture.

This thesis is organized as follows. After the "Introduction" section, "Review of Literature" will be given regarding backgrounds on previous BBB in vitro models, nano/microbubbles used for FUS, and challenges of study cellular interaction with US in vitro. Then the "Methods" section will describe the protocols used during the project. The "Results" section will show how the US-transparent organ-on-chip device was fabricated, the simulation of fluidic flow inside the device, the nanobubble fabrication and characterization, cell culture of the Caco-2 cells and barrier characterization, and finally the disruption of the barrier by BAFUS.

Figure 1 is a schematic of the BAFUS BBB opening setup used for this project where a 1 MHz FUS signal is applied to a US-transparent chip with a cellular barrier and the process is monitored by the subharmonic peak (at 0.5 MHz) of the bubble cavitation using Fast Fourier Transform (FFT) in the frequency domain.

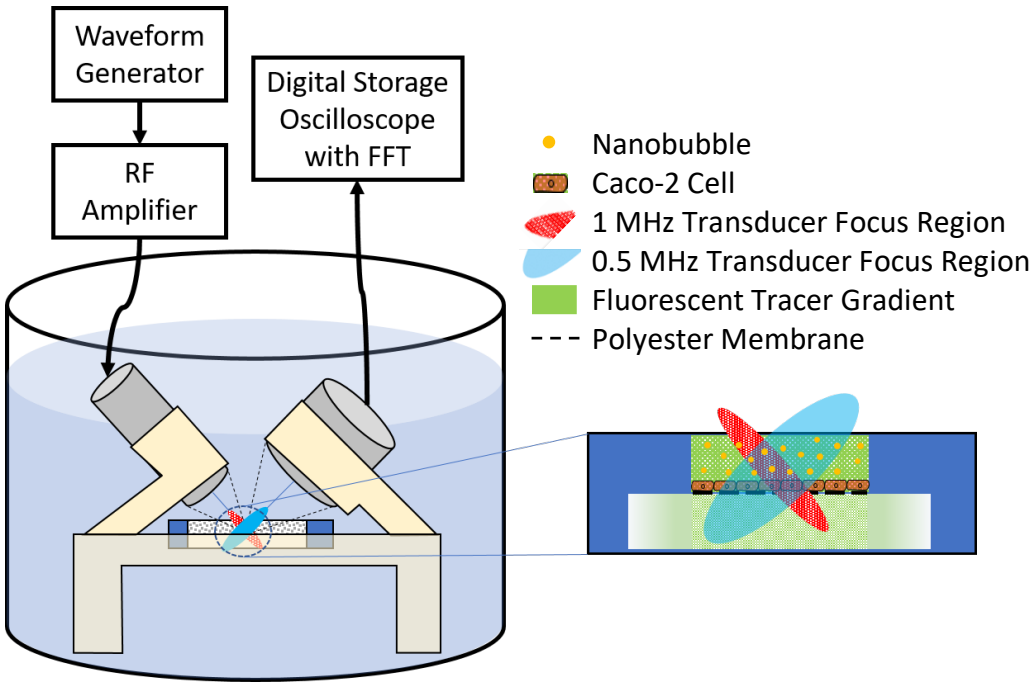

Figure 1: Diagram of BAFUS setup for the BBB-on-Chip. A simple schematic of the BBB-on-Chip is provided on the right that includes key components of the device.

1.3 Summary

This thesis focused on the development of a US-transparent organ-on-Chip platform to study BAFUS BBB opening. A novel US-transparent organ-on-chip device has been fabricated and the transparency of the device window has been confirmed by experiments. Nanobubbles have been fabricated and characterized by cryo-transmission electron microscopy (cryo-TEM). Cavitation of the bubbles under FUS was also

demonstrated. A cellular barrier using Caco-2 cells were established with TEER and permeability values similar to those in the literature. The Caco-2 barrier was successfully established inside the US-transparent chip device, and BAFUS disruption and recovery of the barrier was observed. This newly developed platform can serve as a critical tool for understanding the BAFUS BBB opening process at cellular and molecular level that could lead to a better translation of the BAFUS BBB opening process into clinics for treating brain tumors and other neurological diseases.

CHAPTER 2

REVIEW OF LITERATURE

2.0 *In Vitro* Models of the BBB

Arguably the most basic *in vitro* model of the BBB is the transwell system. Transwells are inserts within wells on a standard well-plate that create apical and basal compartments that are separated by porous membranes. This system is ideal for optimizing culture conditions and selecting the cell types with the tightest tight junction formation before moving on to culture in a device. The inability to achieve physiological shear stress is a drawback of the system. Also, this system alone is not conducive to BAFUS treatment because the plastic plate and wells can scatter the FUS beam to make the FUS power inaccurate. Nonetheless, transwells are very useful for culture optimization purposes.

Several previous efforts have been made to model the BBB for a myriad of reasons including but not limited to pharmaceutical testing, basic physiological understanding, cancer metastasis modeling, and BAFUS treatment modeling. One such device is the humanized dynamic in vitro BBB model (DIV-BBB) which is composed of 50 capillary-like 650 μm diameter porous and hollow propylene fibers submerged in a 13.5 x 9 x 9 mm chamber (30). The device has separate larger luminal and extraluminal chambers in which electrodes are places for TEER measuring capability. Culture was also maintained at a constant flow rate of 1 to 50 mL/min with a pulsatile pump. The authors chose to culture primary human brain microvascular endothelial cells (HBMECs) and human astrocytes (HAs) collected from normal or epileptic brain tissue. The purpose of the study was to evaluate the differences between the BBB physiology, specifically

permeability, TEER, glucose production, and lactate production, of epileptic brain tissue and healthy brain tissue.

A key take-away of the device design is the ability to culture the HBMECs at 6 dyne/cm^2, the physiological brain microvascular shear stress. After an initial slow 1 ml/min adhesion flowrate was applied for 48 hours followed by 1 week of a moderate 4 ml/min flow rate, the DIV-BBB is indefinitely cultured with a 6 ml/min flow rate that was sufficient to achieve physiological shear stress. This functionality is important because maturation of HBMECs has been observed to be largely dependent on shear stress (31). Another key characteristic of the device is the ability to perform TEER measurements on the BBB model as TEER is an important benchmark of BBB tightness seen in transwell models amongst many other models (32).

Another interesting device created by researchers at Temple University, Philadelphia is the microfluidic neonatal blood brain barrier on chip (B^3C) device (33). This device was fabricated using traditional photolithography techniques. It is a PDMS construction plasma bonded to a glass slide substrate. A photomasks and subsequent photoresist development was used to create a central circular tissue compartment surrounded by a vascular ring-shaped channel. A porous wall made of same sized 50 μm pillars with 3 μm gaps separates the central tissue compartment and vascular compartments. Two vascular compartments symmetrically flank the central circular compartment. The objective of the study was to develop an in vitro model for drug testing the BBB and the authors chose to demonstrate the efficacy of the model by measuring the differences between a neonatal and adult BBBs in the B^3C. They cultured either neonatal or adult primary rat astrocytes and brain endothelial cells in the respective channels in the

B^3C and measured Texas Red 70kDa Dextran permeability as well as electrical resistance. The authors were able to measure electrical resistance using a two-point electrode system external to the B^3C and they measured permeability using fluorescence imaging.

The authors note that an important improvement the B^3C has over the DIV-BBB is that the geometry is more akin to physiological capillaries in the brain. They claim that the >600μm diameter fibers used in the DIV-BBB make for an unreasonable flow rate to achieve physiological shear stress, which is wasteful of resources and difficult to achieve and maintain without device leakage and other disruptions. They also claim that their smaller geometrics will cause the cultured cells to behave more like they would in the brain due to there being similar special and geomatic characteristics to the native cell environment.

Another notable feature of this device is the imageability of the cultured cells. Because the device is oriented so that the astrocytes are grown in a compartment separate from the brain endothelial cells but on the same plane, there is a clear divide between the endothelial cells and astrocytes. This enables very clear imaging of the interactions of the modeled BBB. The authors provide beautiful images of endothelial cells squeezing through the pores to interact with the central astrocyte cells. This also makes for straightforward permeability measurements because intensity differences from the vascular channel and tissue channel can be measured on the same image.

There are other microfluidic BBB in vitro models developed besides the two mentioned above. However, most of them are not suitable for BAFUS treatment because

of the device materials used did not have a US impedance matching with the aqueous environment of the cultured cells.

There were also efforts to model BBB interaction with US in vitro. Researchers from the Norwegian University of Science and Technology developed an in vitro model of US-mediated BBB opening (34). This method utilizes a transwell system where primary porcine brain endothelial cells are grown on a polyethylene terephthalate 1 μm porous membrane insert. The insert is then submerged in a degassed deionized water container and exposed to ultrasound. In this design, microbubbles were injected below the insert and let float up to the insert before they were exposed to ultrasound. Permeability and TEER was measured before and after BAFUS treatment. The main drawback to this work seems to be the microbubble exposure method where the bubbles are not confined to a particular compartment. The results for this study were not promising. In fact, they showed a slight decrease in permeability in the cultures after BAFUS treatment, which is the opposite of what is expected. This model did not adequately demonstrate the effects of microbubble assisted ultrasound on the BBB. There currently are no accurate in vitro models of BAFUS treatment found in literature, which suggests there is a significant need for one. This thesis aims to fulfil that need with the production of the ultrasound transparent BBB-on-Chip capable of modeling ultrasound and nanobubble mediated BBB disruption.

2.1 Nano/Microbubbles

Lipid-shell microbubbles have been used in US imaging techniques for decades. They are used as contrast agents to image small blood vessels otherwise not visible (35).

The improved contrast comes from a very different US impedance in gas filled particles than surrounding much denser structures like blood or vessel walls.

More recently, microbubbles have been studied for targeted gene delivery. The inertial cavitation of the bubbles can enhance the permeability of the cellular membrane for better uptake of the drugs (36). The albumin-coated microbubbles adhering to vascular regions were reported with drug delivery even without US (37).

Microbubbles can also undergo stable cavitation under US, which is the repeated expansion and contraction of the bubbles as a result of the generated acoustic pressure waves. The latter have been observed to disrupt tight junction proteins found in tissue structural barriers like the BBB, gut-lining, and respiratory endothelial layers (38). The primary direction of this phenomenon is targeted BBB opening for the purpose of focused drug delivery to the brain. Both stable cavitation and inertial cavitation can disrupt the BBB; however, inertial cavitation has been observed to cause more damage and has less consistent BBB opening when compared to stable cavitation (39).

Microbubbles have been the gold standard for BAFUS treatment and contrast US imaging for years; however, there have been new developments in the nanobubbles space that have received a lot of attention. Interestingly, the Laplace-Young thermodynamics equation implies that nanobubbles could not possibly form in solution because the high capillary pressures from their small diameters would collapse the nanobubbles (40). However, as seen in this thesis and many other papers, the evidence that nanobubble can form in solution is abundant. The current working theory is that nanobubbles can form in heavily gas-saturated solutions because the surface tension is dramatically decreased compared to an unsaturated solution (40). Compared to microbubbles that have diameters

of 1-10 μm, nanobubbles have diameters of approximately 200 nm. The smaller size may have some advantages in reaching small blood vessels in the brain. Most importantly, nanobubbles have been observed to have longer half lives in circulation than microbubbles because of their smaller size (41). This is clinically relevant because it means nanobubbles can be active longer in circulation; therefore, there is more time for BAFUS administration. For these reasons, nanobubbles were selected for the BAFUS treatment studied in this work.

Nanobubbles have five main components in their structure: base phospholipids, anionic phospholipids, an emulsifier, a surfactant, and a gas core (42). Base phospholipids such as DPPC and DPPE make up the majority of the nanobubble's lipid shell. Anionic phospholipids, primarily DPPA, are less prevalent in the shell and function to increase bubble stability and lessen bubble coagulation due to a repulsive negative charge. Emulsifiers such as PEGylated lipids like mPEG-DSPE are also less prevalent in the shell and function to promote stable integration into the bloodstream while avoiding general immune responses like phagocytosis and complement enzyme activation. Surfactants such as Pluronic, propylene glycol, and glycerol are integrated in the bubble solution and lipid shell to prevent coagulation and increase bubble stability. Finally, nanobubbles are filled with an inert gas like octafluoropropane (C_3F_8) to further increase bubble stability and longevity in aqueous solution.

2.2 *In vitro* Setups for Studying Cellular Interaction with US

Traditional tissue culture substates like petri dishes, microplates, or transwells are not ideal for studying cellular interactions with US. High acoustic mismatch between

these materials and the aqueous environment of cells complicates the US administration. The mismatch causes the emergence of unintended “hot spots” of ultrasound energy with uncertainties of up to 700% (45). To address this issue, impedance-matched materials could be used such as hydrogels (46), but hard containers are usually required to hold the sample together, which could also cause inaccurate US intensities at the target. An alternate strategy to avoid US power inaccuracies is to employ a thin membrane encapsulation technique. Thin membranes (~10 μm) that are much smaller than the US wavelength (~1.5 mm for 1 MHz in water) can serve as US-transparent substrates (47). This has not yet been demonstrated in an organ-on-chip platform. Here, we demonstrate this thin membrane phenomenon by making an organ-on-chip with an US-transparent window that allows for accurate US power to be delivered to the cultured cells for the purpose of modeling BAFUS barrier disruption *in vitro*.

2.3 Summary and Conclusions

There have been several *in vitro* models of the BBB produced in the past; however, most do not have the features to allow a quantitative study of the BAFUS BBB opening process. Nanobubbles are a new material for BAFUS BBB disruption that showed additional benefits over its microbubble counterparts and have been adopted in this project. It has been challenging to study cellular interaction with US because of the large acoustic mismatches between the solid culture substrate materials and the aqueous environment of the cells. Our US-transparent device is the first to bring the thin-membrane technology to the organ-on-chip platform.

CHAPTER 3

METHODS

3.0 US-transparent Organ-on-Chip Device Fabrication

3.0.0 Injection Molding

The four PDMS frames that compose the US-transparent chip were created using injection molding. The mold, as seen in the left of Figure 2, was composed of two pieces: a bottom piece with frame reservoirs and a top cover containing injection inlet and vent outlet holes for each frame. The two pieces were held together securely by nuts and bolts. The top-right of Figure 2 shows a mold with nuts and bolts in place, ready for injection. Each mold contains enough frames for 3 complete devices.

Before injection, a ratio of 10:1 PDMS (base to crosslinker by mass) was thoroughly mixed and then placed in a vacuum degasser for at least 30 minutes or until no bubbles were visible. The uncured PDMS was then carefully transferred to a 10 ml syringe with a 25-gauge blunt needle. As seen in the bottom-right of Figure 2, the needle was then placed in the inlet hole of each frame and the syringe was pressed forcefully until the entire frame was filled. If bubbles emerged, more PDMS from the syringe was used to push them out through the pressure outlet hole. Each frame reservoir was filled individually while taking care not to exert too much pressure on the whole mold as that could cause more bubble formation. After injection was complete, the molds were allowed to cure for 48 hours at room temperature (RT), or 24 hours followed by a 1-hour oven treatment at 60 ºC. Once cured, the PDMS frames were carefully removed from the mold and excess PDMS was carefully removed with a sharp blade.

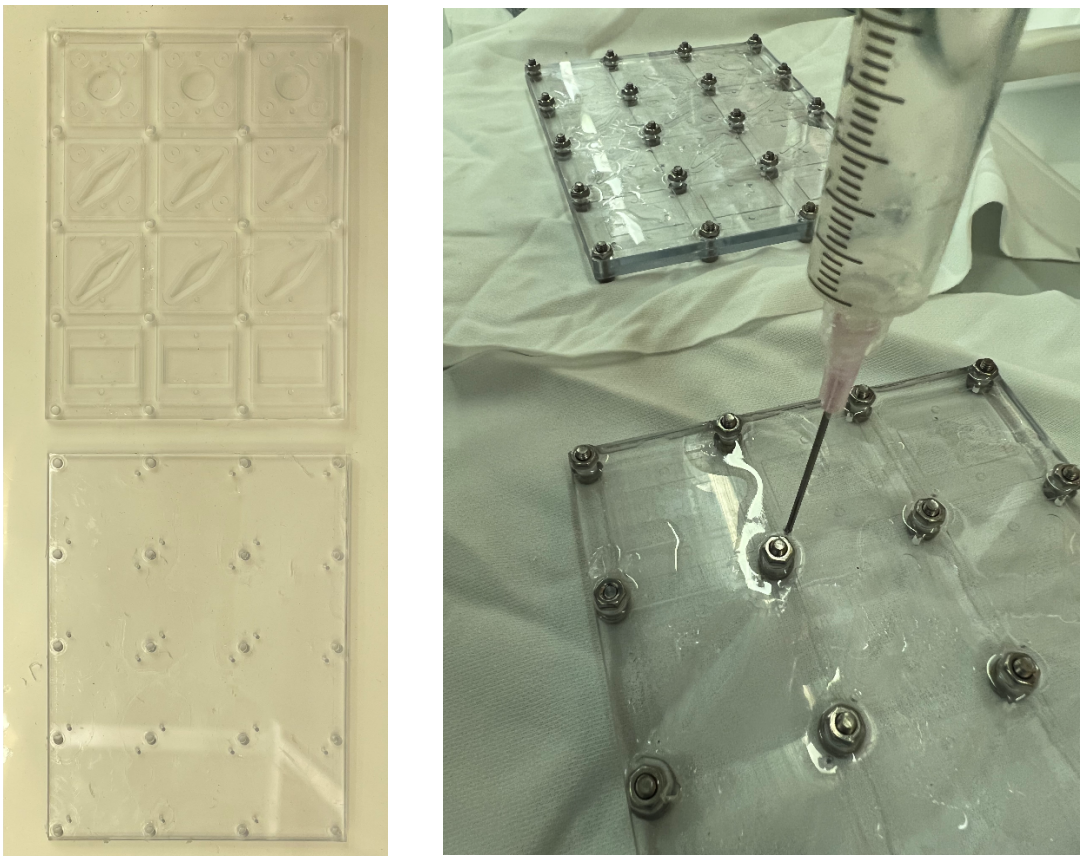

Figure 2: Injection molding of US-transparent chip PDMS frames. To the left is an image of the two pieces of the mold, the frame reservoir (top) and the injection inlet cover (bottom). To the right is an image of the assembled mold being injected with uncured PDMS at a single frame location.

3.0.1 PDMS Membrane Fabrication

The second stage of the US-transparent chip fabrication was to create and bond thin PDMS membranes to the top and bottom channel frames previously molded. As outlined in Figure 3, a silicon wafer was used as a substrate for the process. The wafer was thoroughly cleaned with acetone, then isopropanol, and then methanol before processing. AZ1512 photoresist was used to coat the wafer as a non-adherent coating to allow for the easy removal of fully cured PDMS. The AZ1512 was spun at 4000 RPM and then cured at 90ºC for 90s to achieve a thickness of 1.2 µm (15). PDMS was coated

on top of the cured photoresist by spinning at 3500 RPM to produce the thin membrane thickness of 20 µm (16). The membrane thickness was also confirmed using a Dektak V200-SI stylus profilometer. The PDMS coating was then partially cured at 100 ºC for 30 sec.

To bond the thin PDMS membrane to the middle frames, the middle frames were cleaned with scotch tape first to remove particles on their surfaces and then placed on top of the PDMS thin membrane immediately after the 30 s partial cure. The wafer was then returned to the hot plate and left to continue curing for 10 min at 100 ºC. To ensure the membranes were completely cured, they were let sit at RT overnight, followed by an hour of oven treatment at 60 ºC.

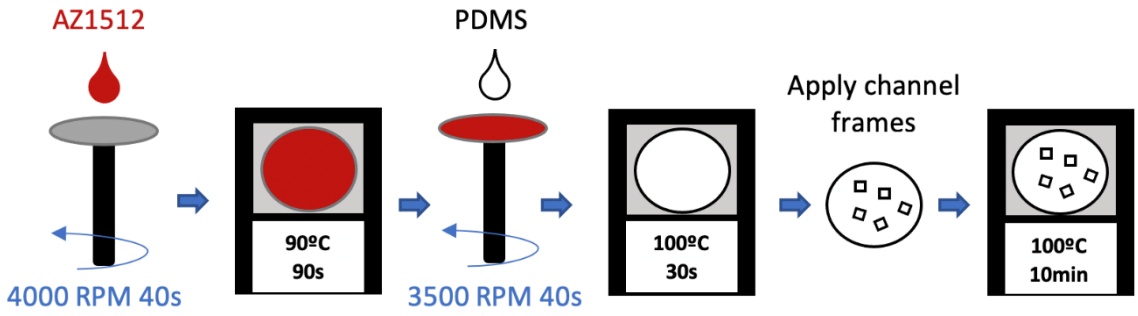

Figure 3: Thin PDMS membrane fabrication. AZ1512 and uncured PDMS were coated on the Si wafer consecutively using different spin coating and baking conditions.

3.0.2 Device Assembly

The final stage of device fabrication was the assembly of individual components. Uncured PDMS was used as a glue to bond the frames and membranes. The uncured PDMS glue was prepared on a Si wafer by spin coating at a slow 500 RPM for 1 min to achieve a 0.5 mm thickness. The surfaces of frames to be bonded were laid onto the wafer to apply the PDMS glue. The frames were then stacked on top of each other in the right order through two guiding holes using two blunt 15-gauge needles, as shown in

Figure 4. The PETE membrane was cut to the same size as the frame (28x28 mm) with guiding holes and inlet/outlet holes using a VersaLaser VLS3.50 laser cutter. After stacking the frame and membrane layers, the device was cured at RT for 24 hours followed by a 1-hour oven treatment at 60 ºC.

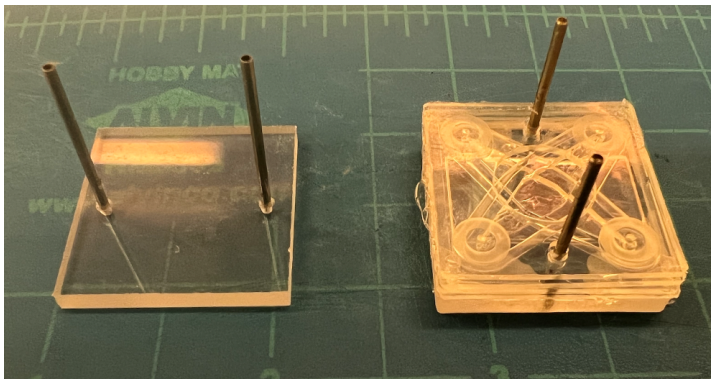

Figure 4: US-transparent chip assembly. On the left is the assembly guide used on its own without an added device. The blunt ended needles go through the two alignment holes on each frame as demonstrated on the right side of the image with the complete device placed on the guide frame by frame.

3.1 Device Characterization

3.1.0 US Transparency Characterization

Figure 5a shows the setup for the device US transparency characterization. A waveform generator (Siglent SDG 1032X) was used to generate 1 MHz burst signal (10ms, 10k cycles) with repetition rate of 1 Hz. The signal was amplified by a 43dB 20W RF amplifier (NP961 from NP Technologies), then sent to a 1 MHz focused Olympus A303S US transducer (15 mm focal length, transverse and axial beam sizes of 1.9 mm and 14 mm). The transducer was mounted on the sidewall of a water tank with the US emission along the long axis of the tank horizontally. During US measurement, the tank was filled with degassed, deionized (DI) water with the transducer submerged. The water

degassing was done by placing the container in a desiccator with -90kPa vacuum for 30 minutes while stirring with a 2-inch magnetic stirrer at 400 RPM. The inner surfaces of the tank were covered by an US absorbing pad (blue material in Fig. 5).

A 1mm needle hydrophone (Precision Acoustics, UK) was used to measure the intensity of the FUS beam. The hydrophone was mounted to a 3D printed holder and a custom XYZ stage was used to change the position of the hydrophone. The measurement was done under the degassed DI water. The holder also had a slot to insert the organ-on-chip device with the US-transparent window of the device between the transducer and the hydrophone to measure any US energy loss due to the membrane window.

To mimic the tilted incident angle of FUS beam in our barrier disruption experiment, the US transparency characterization was also repeated with the device tilted 31° to the transduce-hydrophone axis, as shown in Figure 5b.

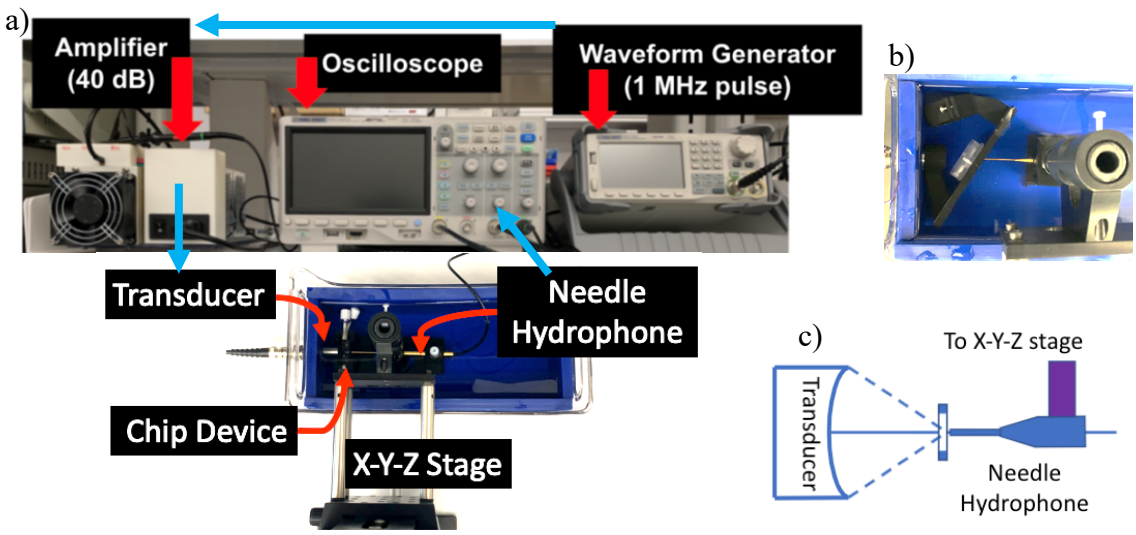

Figure 5: Needle hydrophone characterization setup. (a) The US transparency characterization system. The US-transparent window of the device could be perpendicular (a) or 31° to the transducer-hydrophone axis (b). (c) A schematic drawing of the characterization setup.

3.1.1 Finite Element Modeling

Finite element modeling was used to predict fluid velocity and pressure profiles as well as diffusion gradients in the organ-on-Chip device. The dimensions of the top and bottom channels are provided in Figure 6a. The resulted geometry and mesh generated in COMSOL is provided in Figures 6b and 6c. A 2D mesh and a 3D mesh were created for the laminar flow model, while only a 3D mesh was created for the transport of diluted species model. Both meshes were physics-controlled meshed of quadratic triangular elements auto-generated by the software.

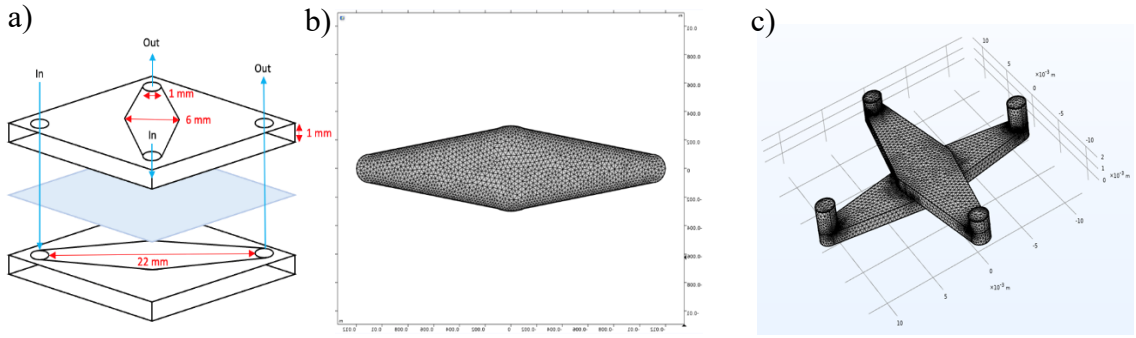

Figure 6: Device Geometry**.** Figure (a) is a diagram of the specific dimensions of the device, (b) is a COMSOL generated physics-controlled mesh of the 2D plane of a single channel, and (c) is a physics-controlled mesh of the whole inner region of the device's channels.

3.2 Nanobubble Fabrication and Characterization

3.2.0 Nanobubble Formulation

Five different lipids were purchased from Avanti Polar Lipids (Birmingham, AL) to fabricate the nanobubbles: 1,2-Dipalmitoyl-sn-glycero-3-phosphate (DPPA), 1,2-dipalmitoyl-sn-glycero-3-phosphocholine (DPPC), 1,2-Dipalmitoyl-sn-glycero-3-phosphoethanolamine (DPPE), 1,2-dibehenoyl-sn-glycero-3-phosphocholine (DBPC),

and 1,2-Distearoyl-sn-Glycero-3-Phosphoethanolamine with conjugated methoxyl poly(ethylene glycol) (DSPE-mPEG). The nanobubble fabrication protocol was adapted from previous studies (22, 23) as follows. A 6:1:2:1 ratio of DBPC (or DPPC) : DPPA : DPPE : DSPE-mPEG was combined and dissolved in chloroform solution. The chloroform was warmed to 80ºC and allowed to evaporate for 3 hours. The lipid powder residue was hydrated in a PBS solution containing 5% glycerol and 0.6% Pluronic L10 at a concentration of 10 mg/ml by stirring at 300 RPM on a 125ºC hot plate for 3 hours. The solution was then aliquoted into smaller rubber septum sealed vials and the air in the vials was replaced with octafluoropropane (C_3F_8). At this point the bubble vials were either stored or activated. To activate the bubbles, the vial was violently shaken in an amalgamator at maximum speed for 45 sec. After amalgamation, a clear divide between white foam, and darker opaque solution appeared when the vial was inverted. Care was taken to only collect the solution that resided below the interface in the darker solution region. This solution was then diluted either 100x or 500x for use in characterization and BAFUS experiments.

3.2.1 BAFUS Setup and Nanobubble Excitation

The BAFUS setup was similar to the US setup used for transparency characterization shown in Figure 5a. However, the needle hydrophone was replaced with a 0.5 MHz Olympus focused receiving transducer. Both the emitting (1 MHz) and receiving (0.5 MHz) transducers were placed in the angled holder shown in Figure 1. A 1 L cylindrical glass beaker layered with US absorbing pads was used to house the setup and degassed DI water. For all BAFUS experiments, the waveform generator was set to a

1 MHz pulse (10,000 cycles and a 1 sec burst period), 100 mVrms, and a 50-ohm load. The oscilloscope was set to read FFT data at a range of 0-10 MHz.

3.2.2 Nanobubble Characterization Using FUS

The bubbles were first diluted to either 100x or 500x in PBS after activation and then injected into the top channel of the device using a syringe pump. Standard 1x PBS was loaded into the bottom channel. Once the device was loaded with PBS and nanobubble solution, the syringe pump was stopped and FUS was delivered while the solutions were static. To characterize the nanobubbles, enhancement (dB) peak height of the 0.5 MHz signal was recorded every second until the peak disappeared using a handheld video camera. Two recipes were characterized: one using DPPC as the primary lipid and the other using DBPC as the primary lipid. The peak height in dB was plotted vs time to produce a peak enhancement curve. The peak of this curve was named signal enhancement. The half-life was measured from time 0 to the time when enhancement decreased by 6 dB from the peak. A decrease of 6 dB from the peak is considered a decrease in half the maximum power generated by bubble stable cavitation. A longevity of nanobubbles was also studied for the 100x DBPC recipe for a constant flow condition with a nanobubble flow rate of 15ml/hr. The 0.5 MHz peak height was plotted during the constant flow until the peak disappeared.

3.2.3 Transmission Electron Microscopy (TEM) Characterization

Finally, the 100x DBPC bubbles were imaged under cryogenic transmission electron microscopy (Cryo-TEM). The general process for preparing cryogenic

transmission electron microscopy samples has been previously described in literature (24). In summary, DBPC recipe samples were placed on a gold microgrid sample and wicked for 6 sec before instantly freezing them to create a vitreous ice on the grid. The duration of wicking determined the thickness of the ice. This vitreous ice was then placed in the transmission electron microscope for imaging. Individual images of the nanobubbles were visualized in the open squares of the sample grid.

3.3 Cell Culture Optimization in Transwells

3.3.0 Transwell culture

A panel of cell types was cultured in transwells to determine the best route to take for BAFUS treatment: in-house differentiated brain endothelial cells from iPSCs, Human Brian Endothelial Cells cell line (HBEC-5i) purchased from ATCC, and Caco-2 cells also purchased from ATCC. Selected iPSC lines were derived from non-diseased subjects with an age range 65-69, high diversity of progeny, and comprehensive molecular data (26). These iPSCs were differentiated into brain endothelial cells (Endo-1) according to a previous study that detailed a specific differentiation protocol (27). Transwell inserts were coated with 1% gelatin for at least 3 hours at 37ºC before seeding any cells. During preliminary panel experiments where multiple cell types were cultured on a single plate, Caco-2 cells were cultured without any prior coating. Transwells were seeded with 33k cells of each cell type with three replicates. Two controls transwells were filled with media, one coated and one uncoated. After Caco-2 cells were selected, their culture was optimized by testing a 10% collagen coating for 3 hours at 37ºC and higher seeding densities of 150k and 200k cells per insert. To culture the endothelial cells, the top and

bottom wells were filled with 200 µl and 500 µl of endothelial cell growth medium (ATCC). Caco-2 cells were cultured with DMEM, 20% FBS, 4.5g/l glucose, 25mM HEPES medium. Cell media was changed every 24 hours or when and measurements were taken.

3.3.1 TEER

STX2 chopstick electrodes and an EVOM2 epithelial voltammeter from World Precision Instruments were used to perform TEER measurements. The electrodes were calibrated with known KCl concentrations according to manufacturer's specifications. The voltammeter was calibrated using a 5000-ohm resistor. To measure TEER, a custom plate cover was machined with holes at each well to allow for electrode insertion while holding all the inserts securely in place. (In previous attempts to measure TEER, the inserts would move and cause the electrode to scrape the cell layer which rendered results unreliable.) The short end of the chopstick electrode was inserted into the top compartment and the longer end was inserted into the bottom compartment to measure the total resistance of the membrane or monolayer. This measured value was multiplied by the area of the membrane in the transwell (0.33 cm^2) to determine the TEER value. TEER values of cell monolayers were further adjusted against controls by subtracting an average background value of the membrane controls.

3.3.2 Permeability

Permeability measurements were conducted in addition to TEER to further characterize monolayer tightness. Two tracer molecules were used: 70kDa-Dextran-

Tetramethyrhodamine (TMR) and 445Da-Lucifer Yellow (LY) from Thermofisher. These tracers were dissolved in a transport buffer containing 0.1 g/l fetal bovine serum (FBS), 4.5 g/l glucose, and 10 mM HEPES in PBS. 100 µl of 10 mM TMR tracer dissolved in transport buffer was placed in the apical compartment of 3 replicate transwells of each cell type as well as a coated and uncoated control. The same was done in a separate well plate with 100 mM of LY in transport buffer. The basal compartments of all wells were filled with 600µl of transport buffer. The plates were then incubated for a total of 1 hour while every 15 minutes, 100 µl was collected and replaced from the basal compartments of all wells. Tracer concentrations in the collected samples were measured using a CLARIOstar plus fluorescence microplate reader.

Permeability coefficients across the membranes with or without cells were calculated using the following equation:

$$P_s = \frac{C_b V_b}{t A C_a} \qquad [1]$$

C_b is the diffused tracer concentration in the basal compartment, V_b is the volume of the basal compartment, t is the time duration, A is membrane surface area between the compartments, and C_a is the loaded tracer concentration in the apical compartment.

3.4 Device culture and BAFUS Treatment

Devices were syringe loaded with 10% collagen and incubated for at least 3 hours at 37 ºC before culture was initiated. The collagen was then rinsed with PBS using a manual syringe. A syringe was then filled with a Caco-2 cell solution with a concentration of 1.5 million cells/ml. This allows for the 100 µl device channel volume to

be filled with 150k cells. The top channel of the devices was carefully filled with the cells while taking care not to introduce bubbles. Complete Caco-2 cell culture medium was loaded into the bottom channel while again trying to avoid bubbles. The devices were then placed in a Petri dish along with ~5 ml of PBS to maintain localized humidity and prevent excess evaporation from the devices. The devices were then cultured in static condition (i.e. without perfusion) for 24 hours.

After 24 hours culture, permeabilities of 70K Dextran-TMR and LY were measured for each device. For a single permeability measurement, concentrated tracer solution (10μM TMR or 100μM LY) was loaded into the top channel of the devices and transport buffer was loaded into the bottom channels. The devices were then allowed to incubate at 37 ºC for 15 minutes. The bottom channel 100μl volumes were then collected and their concentrations were measured using the same methods used in previous transwell experiments. Permeability was then calculated using equation 1.

After the initial permeability measure, the device's top channel was filled with 100x DBPC activated nanobubble solution and the bottom channel was filled with transport buffer. The device was then placed in the ultrasound tank apparatus and nanobubble solution was provided to the top channel at a constant flow of 15ml/hr while BAFUS treatment was administered for a total of 2 minutes for each device. The subharmonic signal detected by the receiving transducer was monitored for the duration of the BAFUS treatment. Additional permeability measurements were made immediately after BAFUS treatment as well as after 24 hour cell culture at 37 ºC inside a CO_2 incubator to allow for recovery from the BAFUS treatment.

CHAPTER 4

RESULTS AND DISCUSSION

4.0 Device Design

A key objective of the BAFUS BBB opening device was to make it US-transparent with minimal energy scattering, reflection, and absorption so that accurate US power can be delivered to cell barriers. This could be achieved with an US window composed of thin membranes. Figure 7a shows the schematic of the device design. The device was composed of four PDMS frames: a top window frame (with holes for US to pass through the center and for inlets and outlets to the channels of the device), a bottom window frame (with a rectangular opening to allow for US to pass at any angle), a top channel frame (with a diamond opening that serves as the top channel of the device and two holes that serve as the inlet and outlet for the bottom channel), and finally a bottom channel frame (with just a diamond shaped opening that forms the bottom channel). The two channel frames were separated by a 12 μm porous polyester polytetrafluoroethylene (PETE) membrane where there was a 6 mm diameter overlapping region between the two channels. To contain the channels, each of the channel frames are sealed off by respective top and bottom 20 μm thick polydimethylsiloxane (PDMS) membranes.

Once the four frames and three thin membranes were assembled in the order shown in Figure 7a, the US-transparent organ-on-chip device was interfaced with an epoxy barb to needle adaptor that was printed using a stereolithography (SLA) 3D printer (part 3 of Figure 7b). The blunt ended needles were inserted into the inlets and outlets of the bottom and top channels; the barbs were used to quickly connect and disconnect the device from tubing when needed. The adaptor also had a large cross shaped opening to

allow for US to pass freely at almost any angle to the device. The PDMS device with the adaptor was then placed in a custom milled clamp (1 and 2 of Figure 7b) and secured by two screws to make a good liquid seal between the adaptor and the PDMS device. The clamp was designed with openings for the barbs to allow for enough room to connect inlet and outlet tubing. The top and bottom parts of the clamp were also designed to have large openings for FUS beam clearance. An image of the completely assembled US-transparent chip including the PDMS device, needle to barb adaptor, and the clamp is shown in Figure 7c.

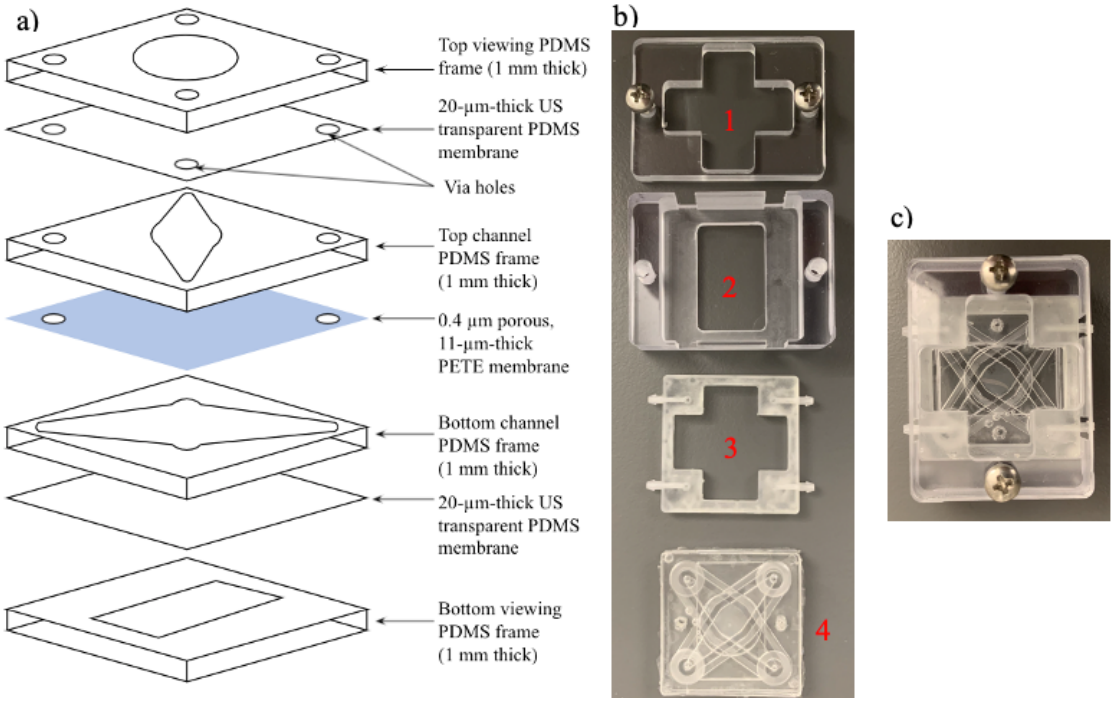

Figure 7: Diagram of exploded Organ-on-Chip and real images for the components and assembled device. A) is a schematic showcasing then layers of the PDMS and PETE constructed Organ-on-Chip. B) is a real image of the surrounding clamp (1/2), the 3D printed barb to needle conversion piece (3) and the PDMS device (4). C) is a real image of the complete device compared to a quarter to demonstrate the relative size.

After the devices were successfully fabricated, they were quality controlled by flowing DI water through them at a flow rate of 1.5 ml/s over 48 hours to ensure no leaks occurred. With current molding supplies, 9 devices were fabricated at a time and consistently about 7/9 devices passed the quality control test. Figure 8 shows an example of a leak free device that passed the test filled with colored dye. It clearly demonstrates the boundaries of the channels and the overlapping region in the middle of the device.

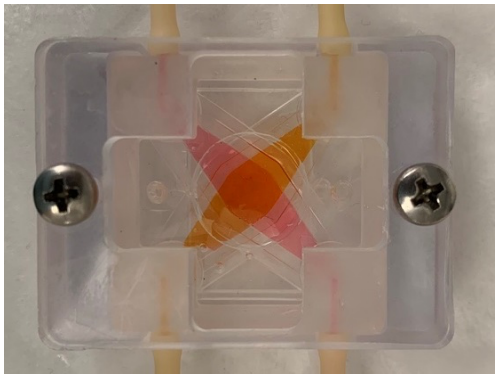

Figure 8: Leak-free device with colored dyes flowing through both channels of the US-transparent chip. Orange dye was flowed through the bottom channel and pink dye was flowed through the top channel.

4.1 Ultrasound Transparency Calculation and Characterization

Figure 9 shows a schematic of US transmission through a thin membrane, where d is the membranes thickness. A theory of US passing through a thin membrane with similar materials on both sides of the membrane (same as in our chip situation) was used to assess the effects of the chip membrane on US transmission (20). The reflection coefficient of the membrane V can be expressed as:

$$V = ({Z_2}^2 - {Z_1}^2)/({Z_1}^2 + {Z_2}^2 + 2iZ_1Z_2 \cot k_{2z}d) \quad (2)$$

where the wave vector $k = \frac{\omega}{c} = \frac{2\pi * f}{c}, k_x = k \sin\theta\,,\ k_y = 0,\ k_z = k\cos\theta$, the impedance $Z_i = \frac{\rho_i c_i}{\cos\theta_i}, i = 1,2,3$ (Z_3=Z_1 for our situation), f and c_i are frequency and speeds of sound in the media, and θ_i are the incident angles.

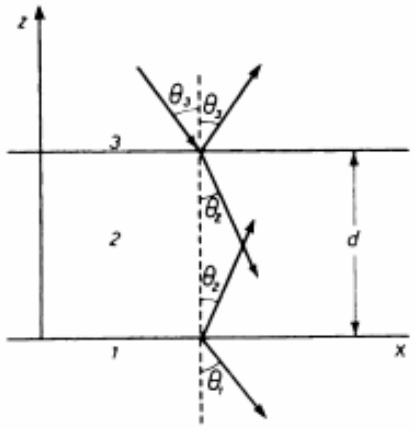

Figure 9: Thin layer model pulled from *Waves of Layered Media* (20).

According to Eq. (2), V is a complex number with both a real and an imaginary component (Eq. 3.1-2). $|V|^2$ is considered for the magnitude of reflection (Eq. 3.3).

$$V_{Real} = \frac{Z_2^4 - Z_1^4}{(Z_2^2+Z_1^2)+4Z_1^2Z_2^2\cot^2 k_{2z}d}, \quad (3.1)$$

$$V_{Img} = \frac{2i\cot(kd)(Z_1^3Z_2 - Z_2^3Z_1)}{(Z_2^2+Z_1^2)+4Z_1^2Z_2^2\cot^2 k_{2z}d} \quad (3.2)$$

$$|V|^2 = V_{Real}^2 + V_{Img}^2 \quad (3.3)$$

The values of parameters used to calculate $|V|^2$ are provided in Tables 1 and 2 respectively. The actual angle of incidence for the ultrasound beam during BAFUS was 31º based on the orientation of the device to the transducer. Two other angles, 0º and 60º, were also calculated.

Table 1: List of known constants converted to standard units

Constant	Value	Unit	SI Conversion	Converted Unit
f	1	MHz	1000000	Hz
c_{PDMS}	1119	m/s	1119	m/s
c_{PETE}	1250	m/s	1250	m/s
c_{H2O}	1490	m/s	1490	m/s
ρ_{PDMS}	969	kg/m^3	969	kg/m^3
ρ_{PETE}	1.38	g/cm^3	1380	kg/m^3
ρ_{H2O}	1.053	g/cm^3	1053	kg/m^3
PSMS membrane thickness (d)	20	µm	0.00002	m
PETE membrane thickness (d)	11	µm	0.000011	m
θ_3 (actual)	31	degrees	0.541	rad
θ_3 (test 1)	60	degrees	1.047	rad
θ_3 (test 2)	0	degrees	0	rad

Table 2: List of calculated constants, equations, and values for three scenarios

Calculated Constant and Equation	Actual (theta3=31)	Test 1 (theta3 = 60)	Test 2 (theta3=0)
$k_{H2O} = \frac{2\pi f}{c_{H2O}}$	4217 s^2/m	4217 s^2/m	4217 s^2/m
$Z_1 = \frac{\rho_{H2O} c_{H2O}}{\cos(\theta_3)}$	1830413 Rayl	3137940 Rayl	1568970 Rayl
$k_{PDMS} = \frac{2\pi f}{c_{PDMS}}$	5615 s^2/m	5615 s^2/m	5615 s^2/m
$\theta_{2PDMS} = \arcsin\left(\frac{k_{H2O}}{k_{PDMS}}\right)\sin(\theta_3)$	0.3972 rad	0.7081 rad	0 rad
$k_{2zPDMS} = k\cos(\theta_{2PDMS})$	5178 s^2/m	4265 s^2/m	5615 s^2/m
$Z_{2PDMS} = \rho_{PDMS} * \frac{c_{PDMS}}{\cos(\theta_{2PDMS})}$	1175832 Rayl	1427477 Rayl	1084311 Rayl
k_{PETE}	5027 s^2/m	5027 s^2/m	5027 s^2/m
θ_{2PETE}	0.4468 rad	0.8133 rad	0 rad
k_{2zPETE}	4533 s^2/m	3454 s^2/m	5027 s^2/m
Z_{2PETE}	2012443 Rayl	3450000 Rayl	1725000 Rayl

Figure 10a-b show how US reflection changes with the membrane thickness for PETE and PDMS respectively. Figure 10c-d are "Zoom-in" views of Figure 10a-b for thin membrane thickness. They show that US reflections are extremely small (< 0.05%) for both membranes at thin thicknesses (~ 10-20 μm). This is consistent with the theory that when $d \to 0, V \to \frac{Z_1 - Z_3}{Z_1 + Z_3} = 0$ (20). Furthermore, normal incident angle shows the highest reflection and reflection decreases with increasing incident angle. The reflection also changes periodically with a period of thickness ~ 500-900 μm. This can be explained by the "half-wave layer" effect, where the membrane would not have any effect on the incident wave (20). If absorption of the membrane is neglected, the transmission of US through the thin membrane can be expected to be:

$$T = 1 - |V|^2 \to 1 \qquad (4)$$

a)

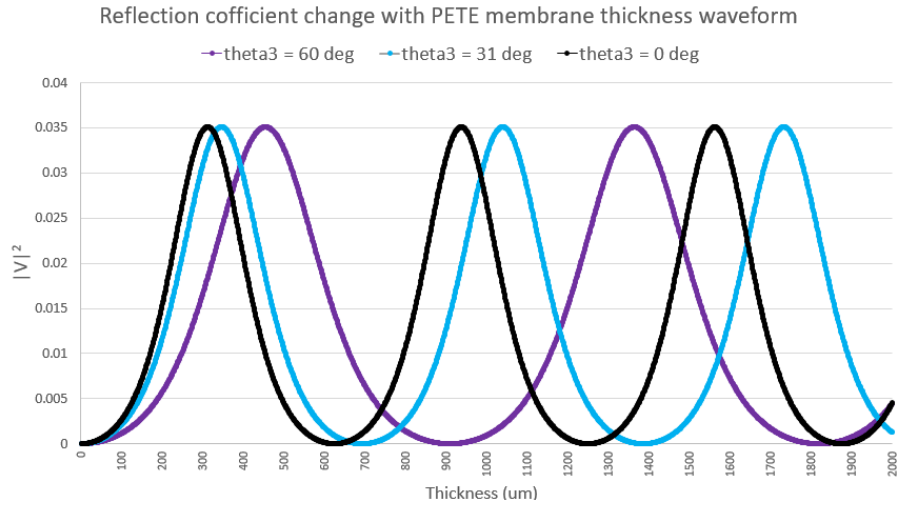

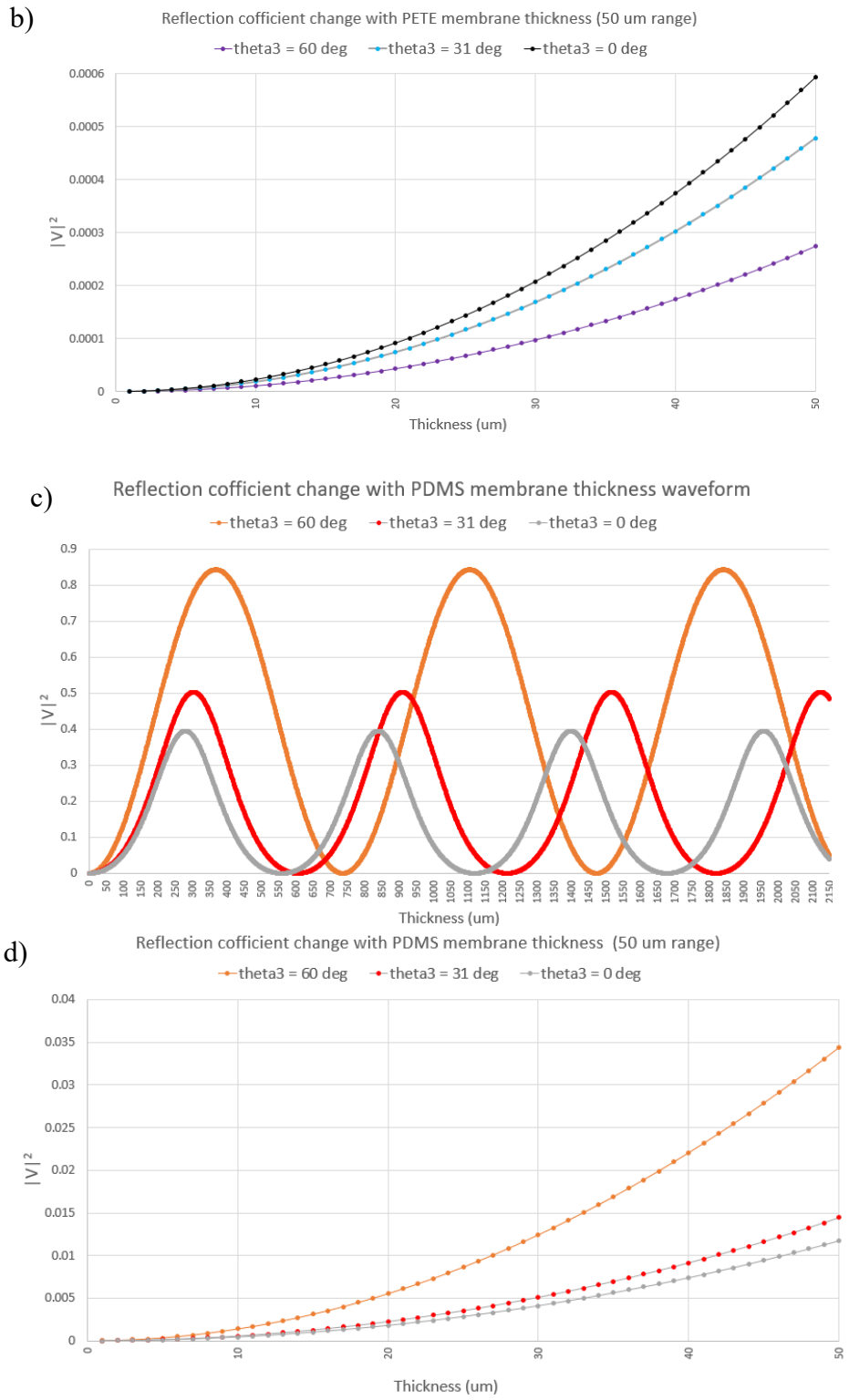

Figure 10: Solutions to modeled reflection through a thin PDMS membrane (c,d) and a thin PETE membrane (a,b). The wave-like graphs at the top of the figure demonstrate the reflection solutions at a large range of membrane thicknesses (0-2mm) while the lower linear graphs are of a smaller 50 µm thickness range.

The high transmission of a thin membrane to a FUS beam was experimentally validated using the setup shown in Figure 5. A needle hydrophone was used to measure the acoustic peak pressures of a FUS beam at its focal point with (P_{peak}') and without (P_{peak}) the chip's US-transparent window placed between the transducer and the hydrophone. The intensity of the sound *I* can be expressed by the sound pressure as:

$$I = \frac{{P_{peak}}^2}{2\rho c} \quad (5)$$

And the transmission of FUS beam through the device window can be expressed as:

$$T = \frac{I'}{I} = \left(\frac{{P_{peak}}'}{P_{peak}}\right)^2 \quad (6)$$

Table 3-4 shows the experiment results of P_{peak} and P_{peak}' for both 0° and 31° incident angles. 6 devices were tested for each case. All device windows showed 100% transmission except two devices (92%) with 31° incident angle. This demonstrated the transparency of the device windows to FUS. The two 92% T could be due to misalignment of the FUS beam to the US-transparent window.

Table 3: Assessing FUS transmission through the device at 0° incident angle

FUS Beam 0° to Device (#)	P_{peak} (MPa)	P_{peak}' (MPa)	% Transmitted
1	0.681	0.681	100
2	0.681	0.681	100
3	0.681	0.681	100
4	0.681	0.681	100
5	0.681	0.681	100
6	0.681	0.681	100

Table 4: Assessing FUS transmission through the device at a 31º incident angle

FUS Beam 31º to Device (#)	P_{peak} (MPa)	P_{peak}' (MPa)	% Transmitted
1	0.377	0.362	92
2	0.377	0.362	92
3	0.362	0.362	100
4	0.362	0.362	100
5	0.362	0.362	100
6	0.348	0.348	100

4.2 Finite Element Modeling of Organ-on-Chip Fluid Dynamics and Diffusion

Finite element modeling can help us better understand the fluid dynamics as well as the diffusion properties of different drugs in the Organ-On-Chip device. Knowing the fluid velocities and pressures at different locations in the channels can help device optimization to create the best possible environment to culture cells. Moreover, modeling diffusion of drugs across the membrane in the device could help our understanding on drugs traveling across the cellular barrier.

4.2.0 Laminar Flow Model

The first model, laminar flow, is based on the Navier Stokes equation, which can describe any type of flow be it laminar or turbulent given the application of the right terms. In this project, the flow in the device is laminar because of the low Reynold number involved. The laminar flow resolved form of the Navier Stokes equation is provided below.

$$\underbrace{\rho\left(\frac{\partial \mathbf{u}}{\partial t}+\mathbf{u}\cdot\nabla\mathbf{u}\right)}_{1}=\underbrace{-\nabla p}_{2}+\underbrace{\nabla\cdot\left(\mu(\nabla\mathbf{u}+(\nabla\mathbf{u})^{T})-\frac{2}{3}\mu(\nabla\cdot\mathbf{u})\mathbf{I}\right)}_{3}+\underbrace{\mathbf{F}}_{4} \quad (8)$$

The equation can be described in four main terms as marked: (1) inertial forces, (2) pressure forces, (3) viscous forces, and (4) external forces applied to the fluid. Regarding the variables and constants, u is the fluid velocity, p is the fluid pressure, ρ is the fluid density, and μ is the dynamic viscosity of the fluid. It is also important to note that this model obeys the continuity principle as momentum is conserved and does not accumulate with time such that:

$$\frac{\partial \rho}{\partial t} + \nabla \cdot (\rho \mathbf{u}) = 0 \tag{9}$$

This model was used in two solutions, a 2D analysis of the y-plane of a single channel, and a 3D model of the entire device. An initial flow velocity set at the inlet boundary conditions was 1mm/s. The solutions, velocity, and pressure profiles in 2D and 3D, are provided in Figure 11 and 12 respectively.

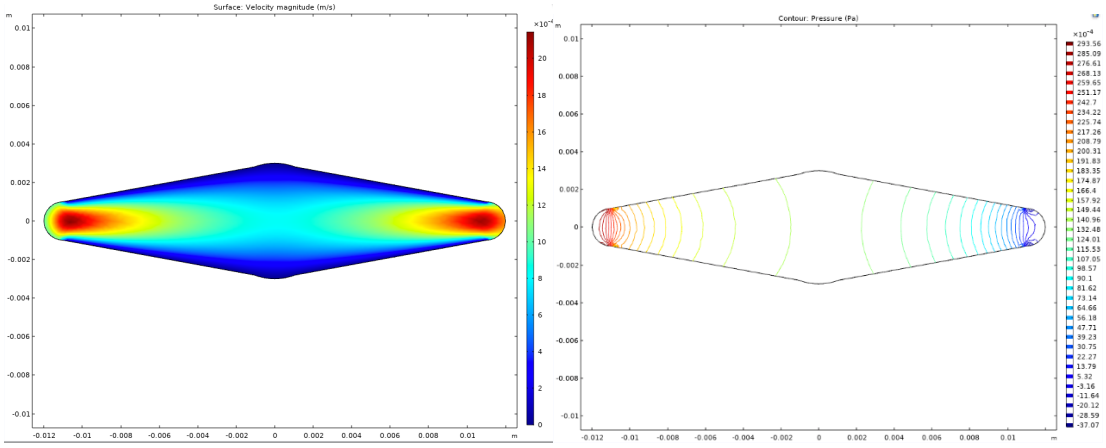

Figure 11: 2D velocity (left) and pressure gradient (right) profile solutions to a laminar flow model of the y-plane of an individual channel based on the mesh generated and shown in Figure 6. Fluid is flowing from the left to right where the inlet and outlet are the leftmost and rightmost arks of the geometry.

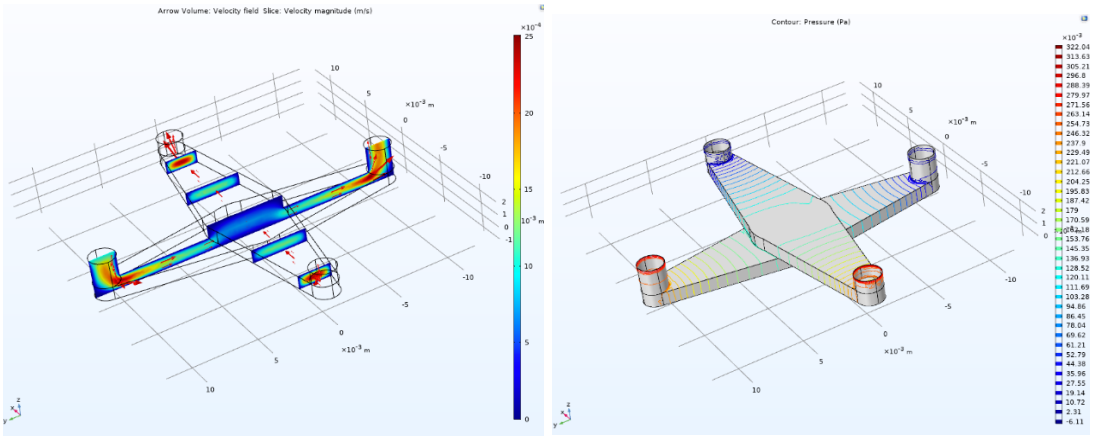

Figure 12: 3D velocity (left) and pressure gradient (right) profile solutions to a laminar flow model of the y-plane of an individual channel based on the mesh generated and shown in Figure 6. The inlets and outlets of this geometry are the bottom-most and top-most upwards projecting cylinder faces respectively.

The small flow velocities in the center window area seen in figures 11 and 12 suggest that physiological shear in the BBB would not be achieved with the current chip geometries and the media circulation would simply be a matter of media replenishment. In fact It was also estimated that even without perfusion, the media in both channels in the device provide sufficient nutrients for a monolayer cell culture in the device for 24 - 48 hours, considering the fact that the medium thickness of 2 mm for the device is comparable to a standard culture flask medium thickness of ~ 2mm. Therefore, for simplicity, static cell culture was used in this project for cultures shorter than 24 - 48 hours.

4.2.1 Transport of Diluted Species Model

The second model solves for the concentration profile in the device as fluorescent tracers pass through the porous membrane. The device geometry was just like the one shown in Figure 6, with an added component, i.e. a thin diffusion barrier between the top

and bottom channels. There are two crucial parameters that characterize this thin diffusion barrier in COMSOL: the membrane thickness d_s and the effective diffusion coefficient across the membrane D_{ei} that can be calculated by the following equation taken from a study on filter membrane characterization (17).

$$D_{ei} = \frac{\varepsilon D_i}{\tau} K_{ri} \quad K_r = \left[1 - \frac{d_m}{d_p}\right]^4, \frac{d_m}{d_p} \leq 1 \tag{10}$$

where ε is the membrane porosity, D_i is the diffusivity of the tracer, τ is the tortuosity, K_r is the restrictive factor, d_m is the size of the molecule, d_p is the size of the membrane pore (18). τ has been approximated as 1 for track etched membrane. ε was taken from the SterilTech membrane manufacturer's site to be 0.3%. The D_i and d_m for 70kDa-dextran, a common fluorescent tracer molecule used to mimic certain chemotherapeutic drugs in permeability studies, were estimated to be 13.9 * 10^{-8} cm^2/s and 3 nm, which leads to a D_{ei} value of 4.046 * 10^{-10} cm^2/s.

Diffusion is similar both across the membrane pore and in the device channels. The equation describing the transport of diluted species model is provided:

$$\nabla \cdot -D\nabla c + u \cdot \nabla c = R \ , \ R = 0 \tag{11}$$

In this case, the diffusion coefficient D is of dextran in water or cell media. Fluid velocity u is a gradient based on initial flow rates and position. Finally, the reaction term R is zero in this model because it is steady state and there is no generation or degradation of dextran.

Multiple 3D solutions to this model were generated in COMSOL for different membrane diffusion constants in attempt to model different states of the organ-on-chip device. The bottom channel was defined with a known concentration of 100 μM and the

top channel had an inlet with an initial 1 mm/s flow velocity and an opposing outlet. The calculated diffusivity of the membrane would be a good model of a device with no cultured cells at all where convection could occur through the membrane's pores. The top of Figure 13 shows the results using parameters for 70 kDa Dextran estimated above. Minimal tracer was observed across the membrane. However, when D_{ei} was increased 1000x (such as LY across a 10% porosity membrane), clear tracer diffusion across the membrane and convection in the top channel were observed, which correctly reflected the physics of the tracer in the device.

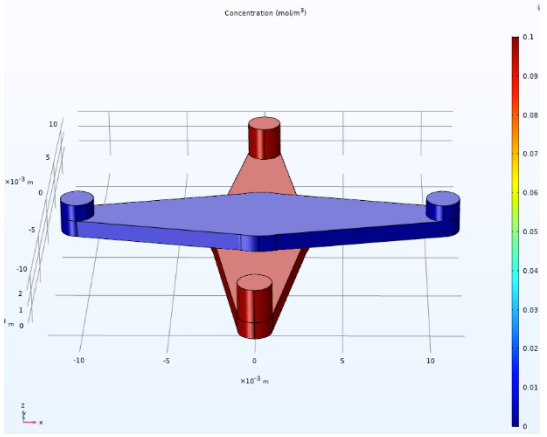

$$D_{ei} = 4.046 * 10^{-10} \frac{cm^2}{s}$$

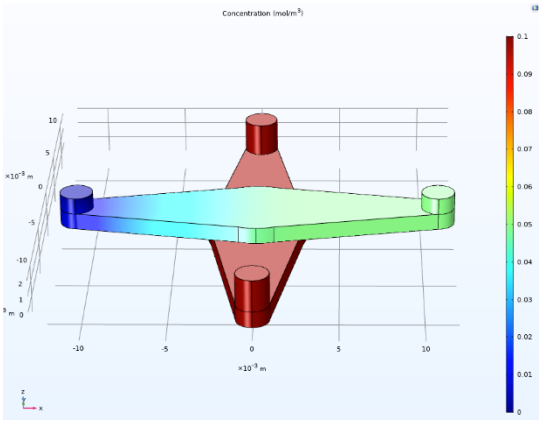

$$D_{ei} = 4.046 * 10^{-7} \frac{cm^2}{s}$$

Figure 13: Solutions to the transport of diluted species model for the Organ-On-Chip device at two different membrane diffusivities. The bottom channel is a set 100 µM concentration and flow moves from left to right at an initial 1mm/s velocity with an inlet concentration of 0 µM.

4.3 Nanobubble Characterization

Nanobubbles were fabricated as described in the Methods. To demonstrate the existence of nanobubble, diluted bubble solution in PBS was loaded into the organ-on-chip device and the BAFUS setup described in Figure 1 and the Methods section was used to excite the bubbles. The acoustic signal of bubble cavitation was monitored using the receiving US transducer, and FFT of the signal was displayed by a digital storage oscilloscope. Figure 14 shows the FFT images of acoustic monitoring of PBS and the DBPC 100x nanobubble solutions loaded into the device. It is clearly seen that PBS only produced fundamental and harmonic peaks (1, 2, 3 … MHz) for the 1 MHz FUS excitation pulse; on the other hand, sub- and super-harmonic peaks (0.5, 1.5, 2.5 … MHz) were observed for the nanobubble solution. Sub- and super-harmonic peaks are characteristic nonlinear signals from bubble cavitation. The observation of these peaks clearly demonstrated the existence of the bubbles in our nanobubble solution.

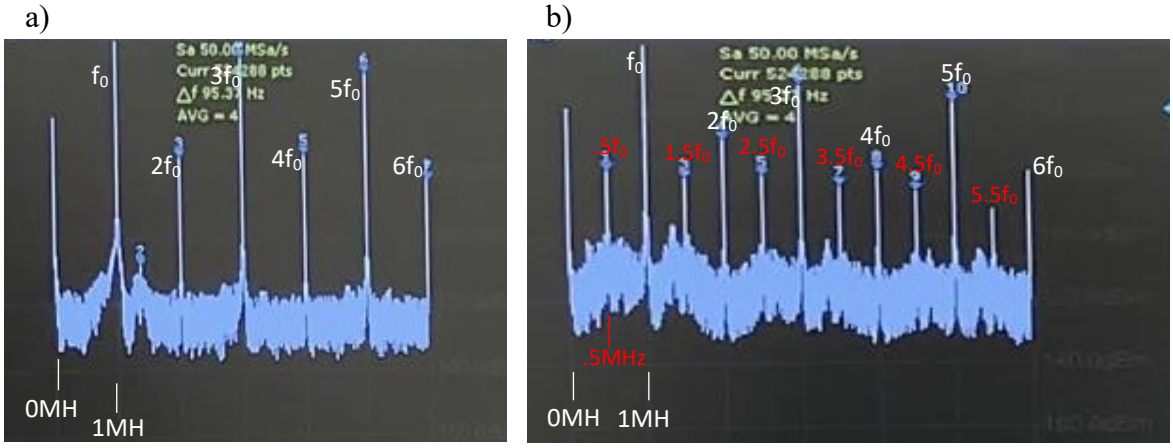

Figure 14: Bubbles were considered detected when sub- and super-harmonic signals emerged. On the left (a) demonstrates the background signal when the device is filled with PBS. The right side (b) demonstrates the signal outputted to the oscilloscope when the top channel is filled with activated bubble solution and the bottom is filled with PBS.

Next, the sub-harmonic peak (0.5 MHz) was used to characterize the cavitation signal and lifetime of the bubbles. A static condition was tested first, i.e. the nanobubble solution was kept in place after loading into the device and the FUS pulses were applied. Figure 15 shows a typical plot of how the sub-harmonic peak height (labeled as signal Enhancement) changed over time for a single loading of a 100x DBPC solution. The decrease of the signal back to the baseline indicates the consumption of the bubbles. The half-life of the bubble solution was defined by a 6 dB decrease from the maximum signal enhancement.

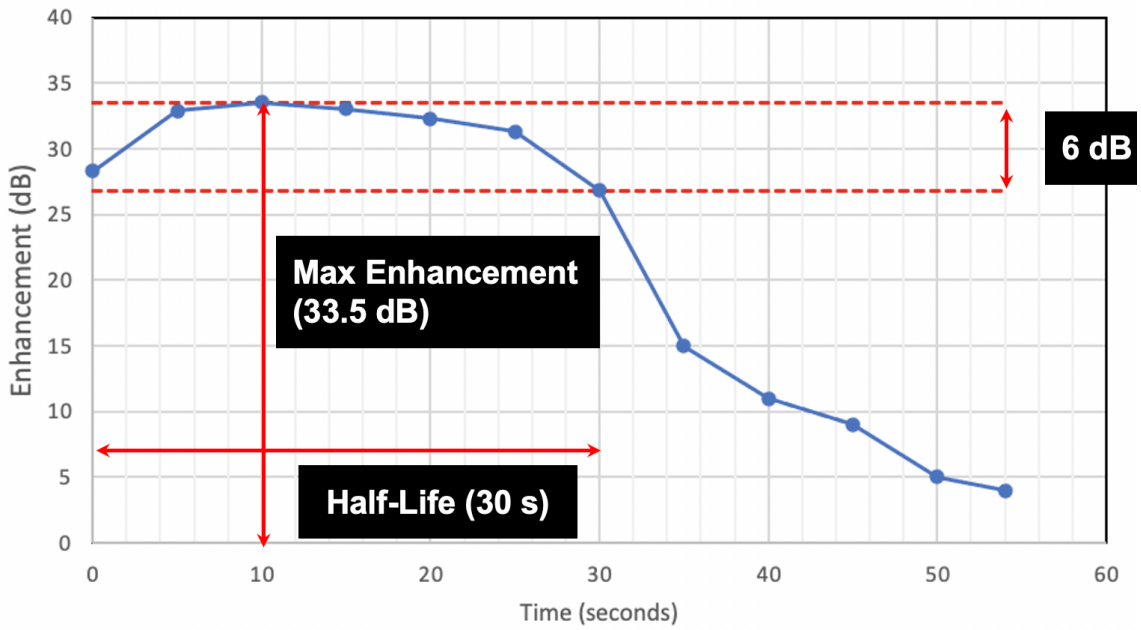

Figure 15: Peak enhancement curve for a 0.5MHz signal produced by stimulated nanobubbles in a 100x dilution DBPC primary lipid recipe. The definitions of signal enhancement as the curve peak height and half-life as the time for the enhancement to decrease by 6 dB are also depicted.

Using this methodology, nanobubble solutions of different recipes and dilution factors were characterized according to their maximum signal enhancements and half-

lives. Figure 16 shows that the DBPC recipe had a stronger cavitation signal and longer half-lives than the DPPC recipe. The 100x and 500x diluted DBPC solutions showed similar maximum sub-harmonic peak heights, but the 100x diluted solution had longer half-life that the 500x diluted solution. Based on these observations, 100x DBPC nanobubble solution was used in the following BAFUS barrier disruption experiments.

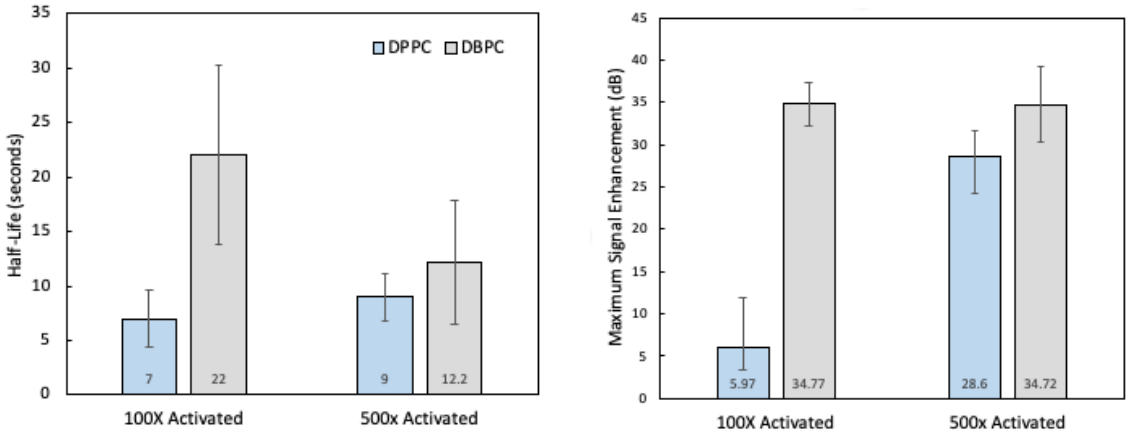

Figure 16: Half-life and signal enhancement characterization of DPPC and DBPC primary lipid recipes at 100x and 500x dilutions.

Further characterizations were also performed for the 100x DBPC nanobubbles under a constant flow (15ml/hr) condition. Figure 17 shows that the maximum sub-harmonic peak could be maintained for more than 5 min, which offers plenty of time for BAFUS therapy to be administered.

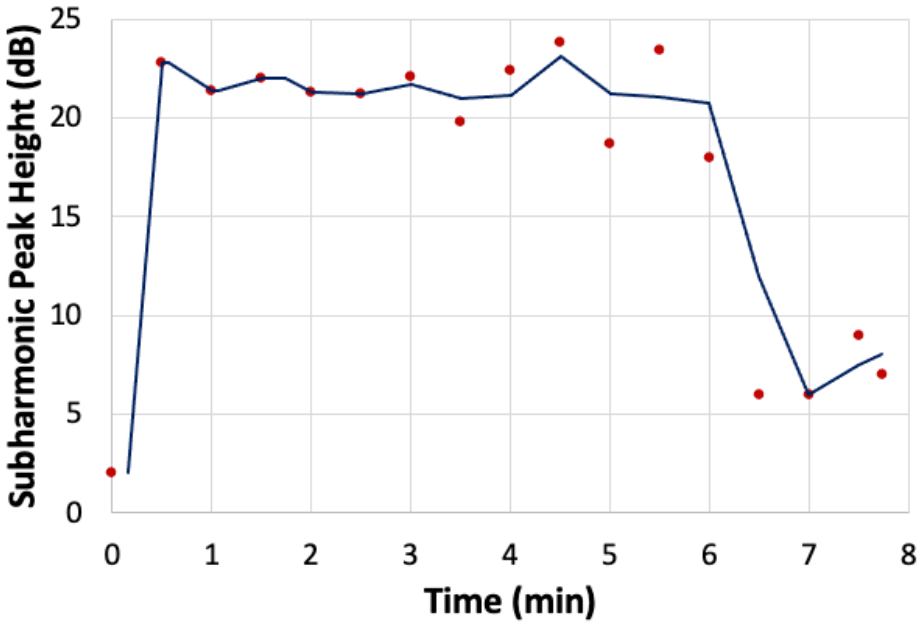

Figure 17: DPBC primary lipid recipe nanobubbles exhibited longevity when diluted 100x under constant 15ml/hr flow.

Finally, shown in Figure 18, Cryo-TEM images were also obtained for the bubbles created using the 100x DBPC recipe. Bubbles similar to those reported in literature, i.e. ~ 200 nm in diameter with lipid bilayer shells and a darkened core, were observed (25).

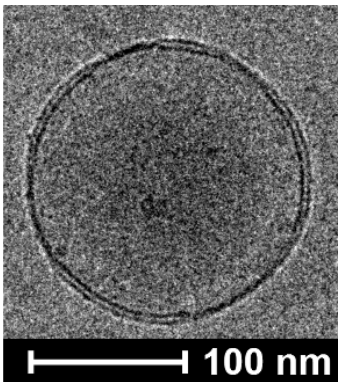

Figure 18: Transmission electron microscopy image of a nanobubble produced by a 100x diluted recipe using DBPC as the primary lipid.

4.4 Transwell Culture Optimization

Transwells are quick and easy models that resemble culture conditions in the device. In transwells, cells grow on PETE membranes with the same 0.4 μm pore size as the membrane in the Organ-on-Chip device. Before optimizing cell culture in the device, transwell culture was performed to optimize cellular barriers using permeability and TEER measurements.

4.4.0 Cell Type Selection from a Panel of Cells

Three cell types (Caco-2, Endo-1, and HBEC-5i) were tested for their ability to form tight cellular barriers. Figure 19 shows TEER measurements of preliminary barrier formation, with Caco-2 cells achieving the highest TEER in just 24 hours. It is important to note that during this experiment the Caco-2 cells and Endo-1 cells began detaching after the 24-hour measurements were made, specifically after changing media. This was attributed to the fact that no collagen coating was applied to the Caco-2 culture surfaces and that the gelatin used to coat the remaining wells was faulty. Collagen was used in later Caco-2 culture optimization experiments. Figure 20 further confirmed that Caco-2 cells achieved permeabilities that were significantly lower than other barriers (HBEC-5i and Endo-1 cells) for LY and TMR tracers. These preliminary results led us to choose Caco-2 cells for BAFUS barrier disruption studies.

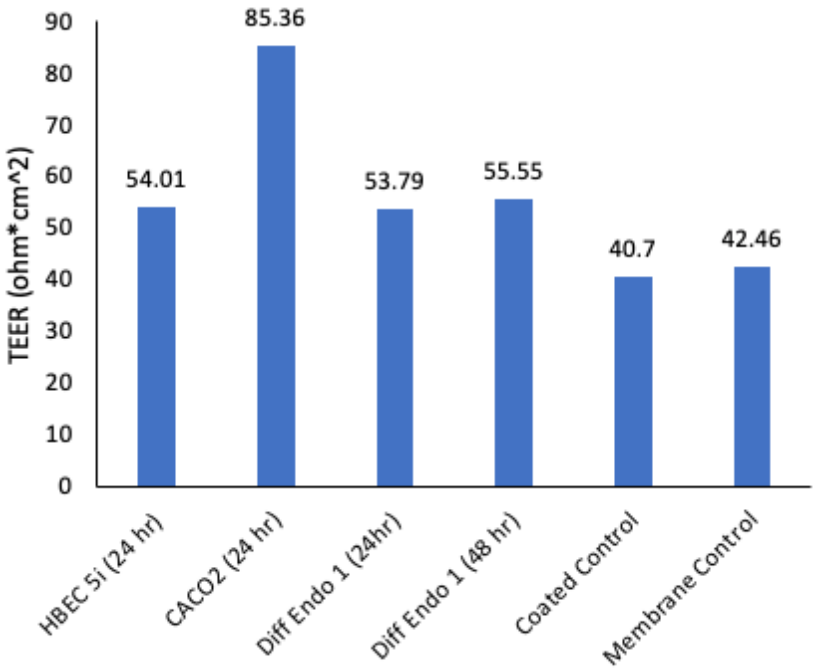

Figure 19: Average TEER measurements for monolayers of a panel of cell types including HBEC-5i, Caco-2, and an in-house differentiated brain endothelial cell type. All measurements were made after 24 hours with the exception of the differentiated cell type for which a 48 hour measurement was also made. The TEER values displayed in this figure were not standardized to the membrane and coated controls, which is why the values for the controls are also provided.

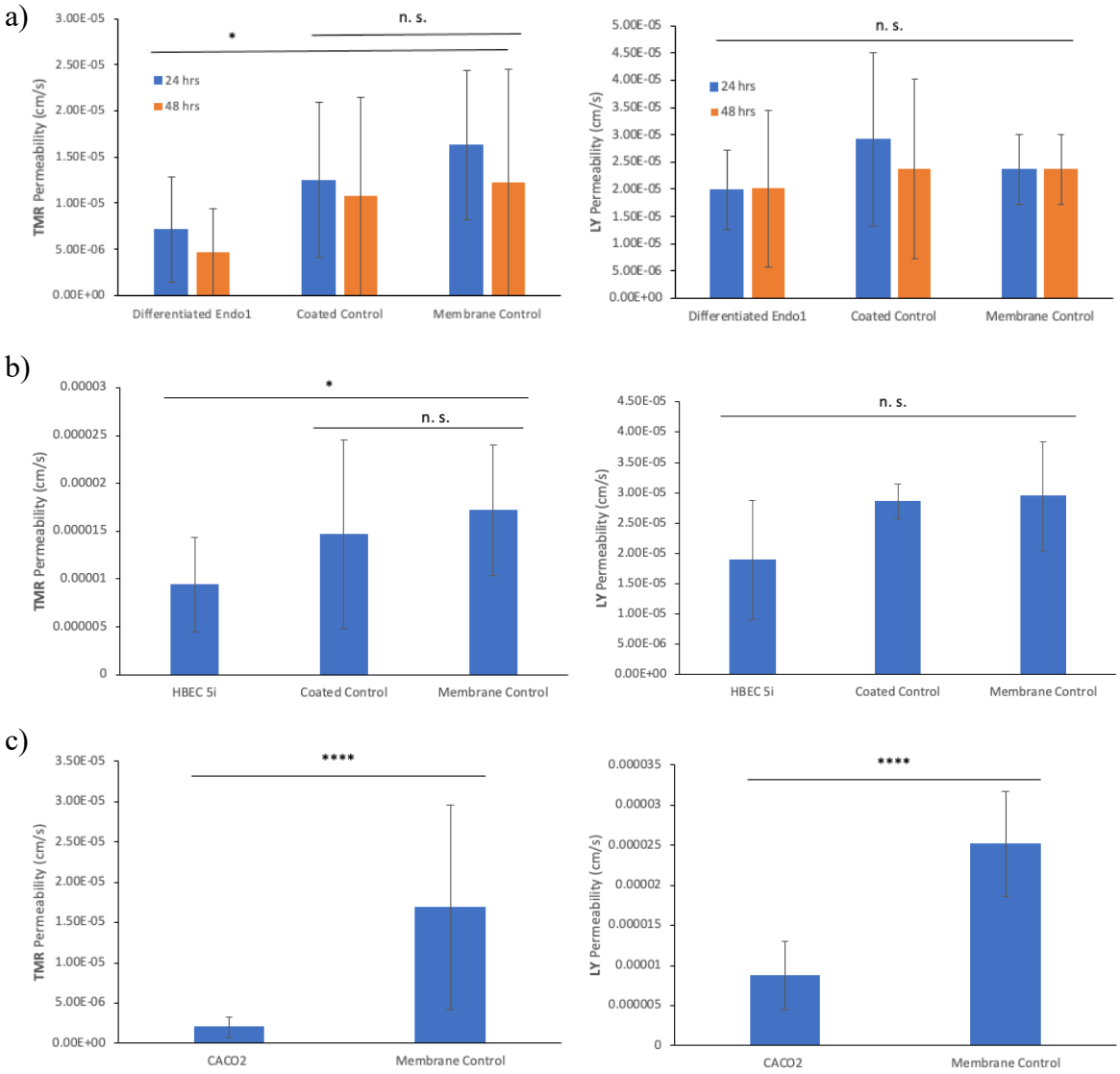

Figure 20: Permeability measurements for a panel of cell types grown in transwells. Figures a, b, and c are 70kDa Dextran-TMR (left) and Lucifer Yellow (right) permeability measurements of in-house differentiated brain endothelial cells, HBEC-5i cells, and Caco-2 cells, respectively. A paired, equal variance T-test was performed for all figures where **** indicates a p-value < 0.0005, * indicates a p-value < 0.5, and n.s. indicates the p-value was > 0.05.

4.4.1 Optimization of Caco-2 Culture

The Caco-2 cell culture protocol was further optimized based on literature to obtain better barrier properties for BAFUS barrier disruption study. Literature has shown that high seeding density can lead to high TEER values (150-400 ohms*cm^2) in just 24-72 hours (28, 29). The protocols mentioned in these studies also used a 10% collagen solution coating on the substrate. These conditions were tested in this project. Figure 21 shows that indeed, TEER values of approximately 300 ohm*cm^2 were achieved within 24 hours for seeding densities of 150k and 200k cells/insert. There was a general decrease in TEER over the three-day culture period for both seeding densities, indicating an optimal culture period of 24 hours for BAFUS treatment.

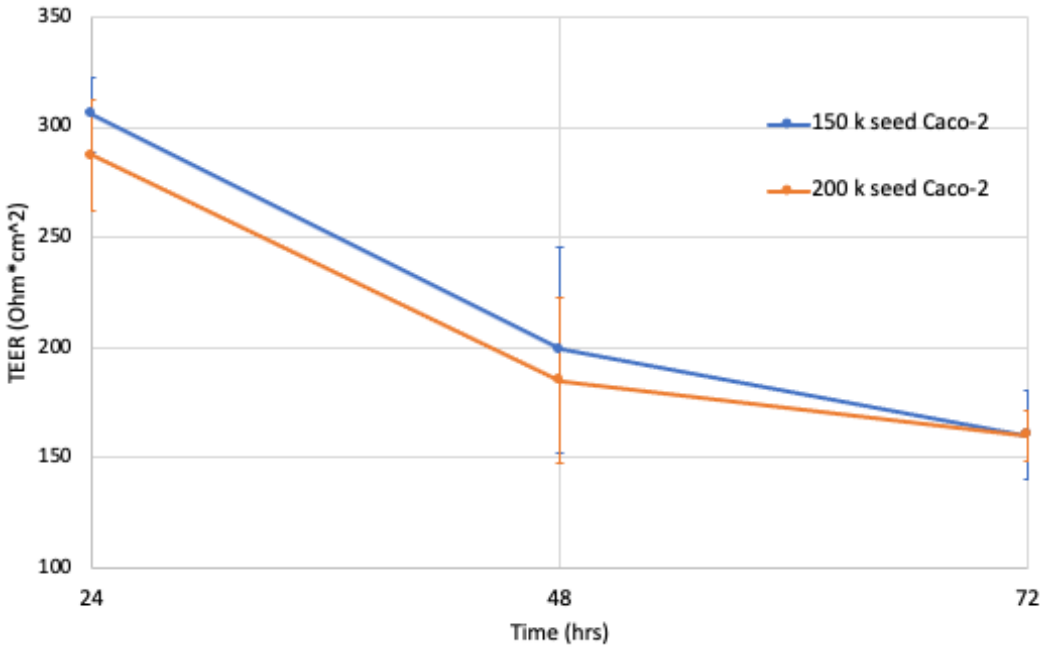

Figure 21: TEER measurements over 72 hours for 150k and 200k initial transwell seedings of Caco-2 cells. These data were standardized against an average coated and uncoated control data set.

Figure 22 shows that Caco-2 barriers from both seeding densities significantly decreased the permeabilities to TMR and LY tracers at 24 and 48 hour time points, and no significant difference between the two seeding densities was observed. Based on these observations, the 150k cell/insert was chosen for further studies as it requires less cells.

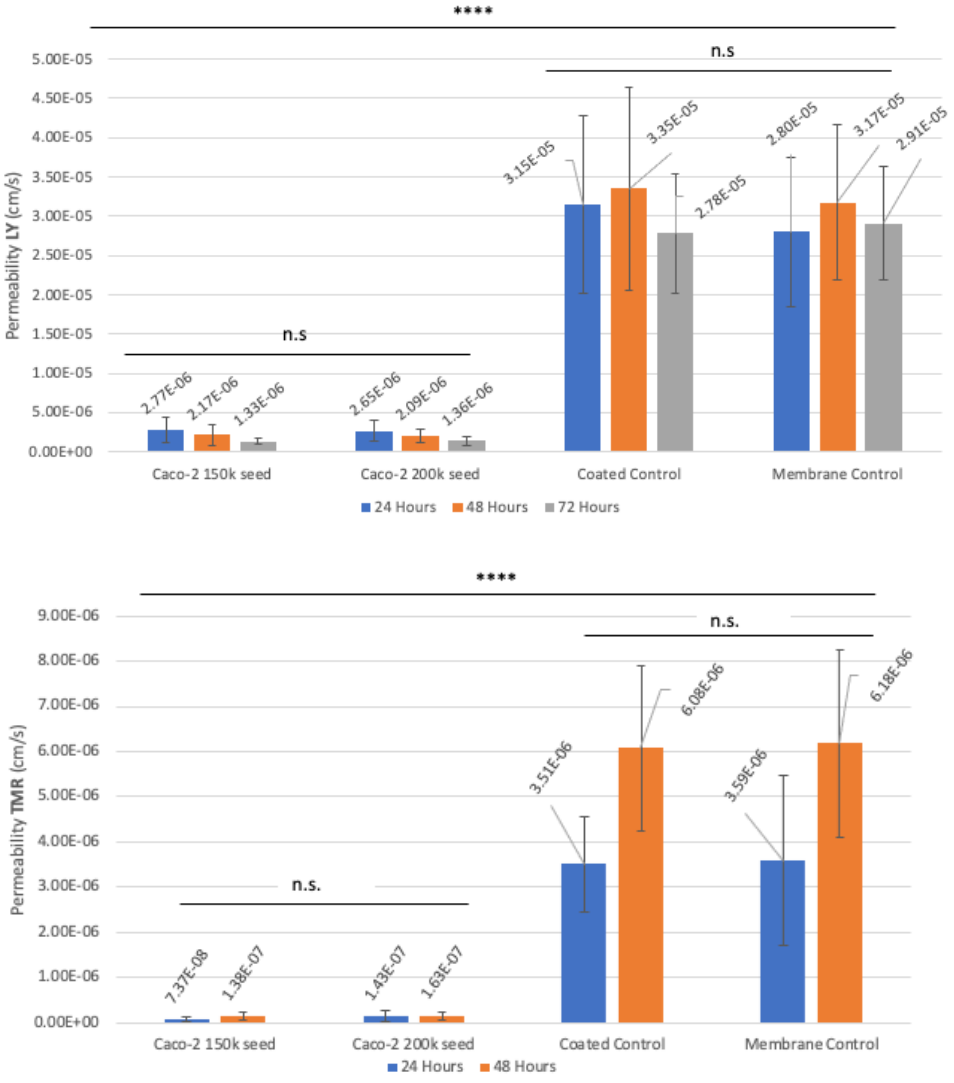

Figure 22: Permeability Lucifer yellow (top) and 70k-Dextran-TMR (bottom) in a transwell system with control membranes or membranes layered with Caco-2 cells. A paired, equal variance T-test was performed for all figures where **** indicates a p-value < 0.0005 and n.s. indicates the p-value was > 0.05.

4.5 Caco-2 Barrier in US-transparent Chip and BAFUS Barrier Disruption

After transwell barrier optimization, 150k Caco-2 cells were loaded into the chip device to form the barrier. Cellular barrier was visible at 24 hours by phase contrast microscopy, as shown in Figure 23 (baseline). Then 100x DBPC solution was flowed through the device and BAFUS treatment was applied using 1 MHz pulses (100 mVrms, 10k cycles/pulse and 1 Hz pulse frequency) for 2 mins. Figure 23 also shows that the phase contrast microscopy images of the cellular barrier immediately and 24 hrs after BAFUS treatment. No significant damage of the barrier was visible.

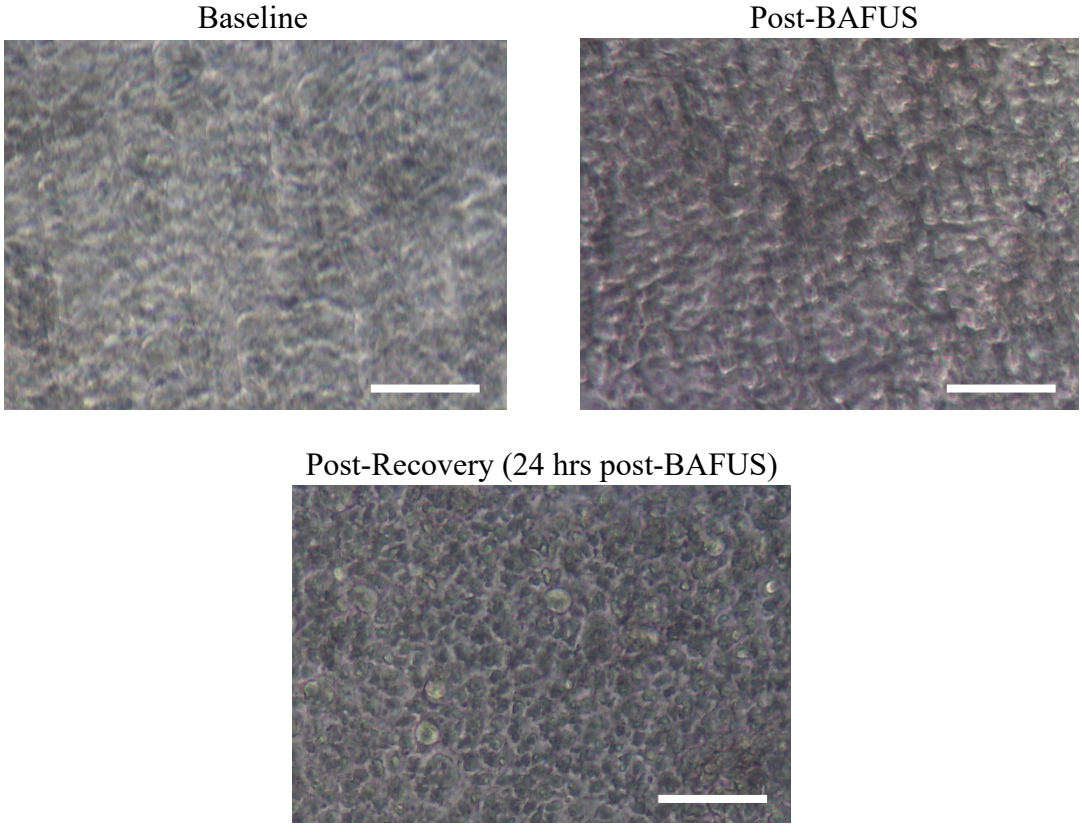

Figure 23: Contrast images of Caco-2 culture in the US-transparent Chip at baseline, post-BAFUS, and post-recovery. Images were taken at 10x magnification, and the white scale bar is 100µm in all three images.

Even though similar phase contrast images were obtained, permeability of the barrier to molecular tracer could change dramatically after the BAFUS treatment. Figure 24 shows that a 100-fold increase in permeability to the 70k-Dextran-TMR tracer from baseline was observed immediately after the BAFUS treatment, demonstrating the disruption of the barrier property. This disruption was observed to be recovered by culturing the cellular barrier over time, as shown by the 10-fold decrease of the permeability after 24 h of barrier culture post BAFUS treatment.

Even though clear barrier disruption and recovery were observed for the 70k-Dextran-TMR tracer, the difference between LY tracer permeability post BAFUS and post recovery culture was not so pronounced. This could be due to the much smaller molecular size of LY and the differentiate tightness of the cellular barrier for different sized molecular tracers. It could take a longer culture period to restore baseline barrier tightness and observe a more pronounced difference between LY post-BAFUS and post-recovery permeability measurements.

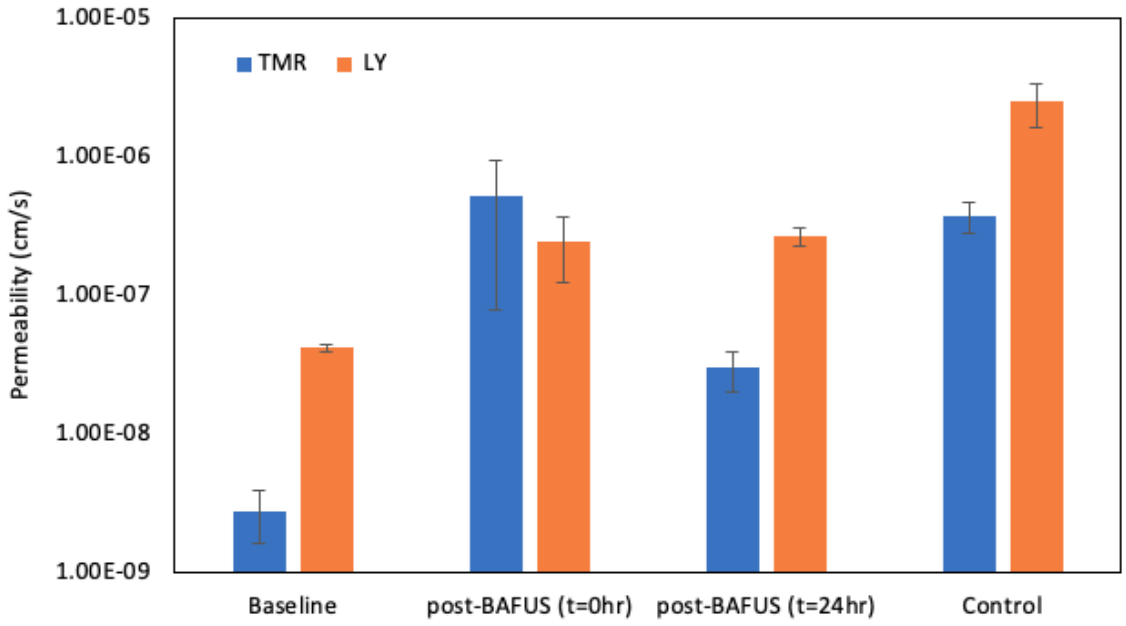

Figure 24: Baseline, post-BAFUS, recovery, and control permeability measurements for Caco-2 cells grown in the US-transparent chip. Baseline measurements were taken 24 hours after initial cell seeding. BAFUS was administered immediately following the 24-hour baseline permeability measurement, which was followed by the post-BAFUS permeability measurement. The post-recovery measurement was taken 24 hours after BAFUS treatment. The control measurements were made in uncoated devices with no cell culture. The baseline, post-BAFUS, and post-recovery measurements were averages from two devices. The control data were averages from 6 runs.

Lastly, the baseline permeability values of the devices without cells were much smaller than those from transwells. This is unexpected considering similar membranes were used for both cases in terms of the porosity, pore size, and membrane thickness. This observed discrepancy may be explained by the fact that PDMS is also a porous material and could absorb small molecules (43).

CHAPTER 5

CONCLUSION AND FUTURE WORK

US-transparency is a key feature of our Organ-on-Chip platform that enables quantitative linkage between BAFUS power by different parameters and the disruption of the cellular barrier. In this thesis, US-transparent organ-on-chip devices based on thin membranes have been designed and fabricated. The US transparency of the thin membrane window of the device was theoretically calculated and verified by experiments. Nanobubbles were fabricated and showed bubble cavitation inside the device, as demonstrated by the sub- and super-harmonic peaks from acoustic monitoring. FEM was used to understand the flow profile and molecular diffusion inside the device. A fast Caco-2 barrier formation protocol was demonstrated based on literature, and barrier disruption by BAFUS and subsequent recovery were observed in Caco-2 seeded US-transparent chip device.

The current thesis establishes a foundation for an US-transparent Organ-on-Chip platform that could be used to study BAFUS disruption of BBB. Towards building such an *in vitro* model, different BAFUS parameters on barrier disruption will be studied. A setup will be developed to allow real-time imaging of the cellular barrier during disruption. Fluorescent staining will be used to interrogate different barrier molecules, such as tight junction molecules. Finally, iPSC-derived HBMECs and co-cultures of astrocytes and pericytes with different genetic makeups from our collaborators will be used to study individual differences of barrier disruption due to genetic differences.

REFERENCES

1. Wolff, A., Antfolk, M., Brodin, B., & Tenje, M. (2015). In Vitro Blood–Brain Barrier Models—An Overview of Established Models and New Microfluidic Approaches. *Journal of Pharmaceutical Sciences*, *104*(9), 2727–2746. https://doi.org/10.1002/jps.24329

2. Pardridge, W. M. (2012). Drug transport across the blood–brain barrier. *Journal of Cerebral Blood Flow & Metabolism*, *32*(11), 1959–1972. https://doi.org/10.1038/jcbfm.2012.126

3. Abrahao, A., Meng, Y., Llinas, M., Huang, Y., Hamani, C., Mainprize, T., Aubert, I., Heyn, C., Black, S. E., Hynynen, K., Lipsman, N., & Zinman, L. (2019). First-in-human trial of blood–brain barrier opening in amyotrophic lateral sclerosis using MR-guided focused ultrasound. *Nature Communications*, *10*(1), 4373. https://doi.org/10.1038/s41467-019-12426-9

4. Izadifar, Z., Babyn, P., & Chapman, D. (2019). Ultrasound Cavitation/Microbubble Detection and Medical Applications. *Journal of Medical and Biological Engineering*, *39*(3), 259–276. https://doi.org/10.1007/s40846-018-0391-0

5. Aryal, M., Arvanitis, C. D., Alexander, P. M., & McDannold, N. (2014). Ultrasound-mediated blood-brain barrier disruption for targeted drug delivery in the central nervous system. *Advanced Drug Delivery Reviews*, *0*, 94–109. https://doi.org/10.1016/j.addr.2014.01.008

6. Norén, E., Mellander, M.-R., Almer, S., & Söderman, J. (2018). Genetic Variation and Gene Expression Levels of Tight Junction Genes Indicates Relationships Between PTEN as well as MAGI1 and Microscopic Colitis. *Digestive Diseases and Sciences*, *63*(1), 105–112. https://doi.org/10.1007/s10620-017-4857-7

7. Yamaura, Y., Chapron, B. D., Wang, Z., Himmelfarb, J., & Thummel, K. E. (2016). Functional Comparison of Human Colonic Carcinoma Cell Lines and Primary Small Intestinal Epithelial Cells for Investigations of Intestinal Drug Permeability and First-Pass Metabolism. *Drug Metabolism and Disposition*, *44*(3), 329–335. https://doi.org/10.1124/dmd.115.068429

8. Endo-Takahashi, Y., & Negishi, Y. (2020). Microbubbles and Nanobubbles with Ultrasound for Systemic Gene Delivery. *Pharmaceutics*, *12*(10), 964. https://doi.org/10.3390/pharmaceutics12100964

9. Zhang, D. Y., Dmello, C., Chen, L., Arrieta, V. A., Gonzalez-Buendia, E., Kane, J. R., Magnusson, L. P., Baran, A., James, C. D., Horbinski, C., Carpentier, A., Desseaux, C., Canney, M., Muzzio, M., Stupp, R., & Sonabend, A. M. (2020). Ultrasound-mediated Delivery of Paclitaxel for Glioma: A Comparative Study of Distribution, Toxicity, and Efficacy of Albumin-bound Versus Cremophor Formulations. *Clinical Cancer Research*, *26*(2), 477–486. https://doi.org/10.1158/1078-0432.CCR-19-2182

10. Greish, K. (2010). Enhanced Permeability and Retention (EPR) Effect for Anticancer Nanomedicine Drug Targeting. In S. R. Grobmyer & B. M. Moudgil (Eds.), *Cancer Nanotechnology: Methods and Protocols* (pp. 25–37). Humana Press. https://doi.org/10.1007/978-1-60761-609-2_3

11. Peyman, S. A., McLaughlan, J. R., Abou-Saleh, R. H., Marston, G., Johnson, B. R. G., Freear, S., Coletta, P. L., Markham, A. F., & Evans, S. D. (2016). On-chip preparation of nanoscale contrast agents towards high-resolution ultrasound imaging. *Lab on a Chip*, *16*(4), 679–687. https://doi.org/10.1039/C5LC01394A

12. Ebina, K., Shi, K., Hirao, M., Hashimoto, J., Kawato, Y., Kaneshiro, S., Morimoto, T., Koizumi, K., & Yoshikawa, H. (2013). Oxygen and Air Nanobubble Water Solution Promote the Growth of Plants, Fishes, and Mice. *PLOS ONE*, *8*(6), e65339. https://doi.org/10.1371/journal.pone.0065339

13. *Brain Tumor—Statistics*. (2012, June 25). Cancer.Net. https://www.cancer.net/cancer-types/brain-tumor/statistics

14. *American Cancer Society | Information and Resources about for Cancer: Breast, Colon, Lung, Prostate, Skin*. (n.d.). Retrieved January 28, 2022, from https://www.cancer.org/cancer/brain-spinal-cord-tumors-adults/detection-diagnosis-staging/survival-rates.html.

15. *AZ 1512 HS*. (n.d.). EPFL. Retrieved February 17, 2022, from https://www.epfl.ch/research/facilities/cmi/process/photolithography/photoresist-selection/az-1512-hs/

16. Baëtens, T., & Arscott, S. (2019). Planarization and edge bead reduction of spin-coated polydimethylsiloxane. *Journal of Micromechanics and Microengineering*, *29*(11), 115005. https://doi.org/10.1088/1361-6439/ab3b18

17. Kruczek, B. (2015). Diffusion Coefficient. *Encyclopedia of Membranes*, 1–4. https://doi.org/10.1007/978-3-642-40872-4_1993-1

18. Alkhudhiri, A., & Hilal, N. (2018). Membrane distillation—Principles, applications, configurations, design, and implementation. *Emerging Technologies for Sustainable Desalination Handbook*, 55–106. https://doi.org/10.1016/b978-0-12-815818-0.00003-5

19. DeStefano, J. G., Jamieson, J. J., Linville, R. M., & Searson, P. C. (2018). Benchmarking in vitro tissue-engineered blood–brain barrier models. Fluids and Barriers of the CNS, 15(1). https://doi.org/10.1186/s12987-018-0117-2.

20. Brekhovskikh, L. (2012). *Waves in Layered Media*. Elsevier.

21. Wang, H., Cao, W., Zhou, Q., & Shung, K. K. (2003). Characterization of ultra-thin quarter-wavelength matching layers of high frequency ultrasonic transducers. *IEEE Symposium on Ultrasonics, 2003*, *1*, 1048-1051 Vol.1. https://doi.org/10.1109/ULTSYM.2003.1293579

22. Lapin, N. A., Gill, K., Shah, B. R., & Chopra, R. (2020). Consistent opening of the blood brain barrier using focused ultrasound with constant intravenous infusion of microbubble agent. *Scientific Reports*, *10*(1), 16546. https://doi.org/10.1038/s41598-020-73312-9

23. Cheng, B., Bing, C., Xi, Y., Shah, B., Exner, A. A., & Chopra, R. (2019). Influence of Nanobubble Concentration on Blood–Brain Barrier Opening Using Focused Ultrasound Under Real-Time Acoustic Feedback Control. *Ultrasound in Medicine & Biology*, *45*(8), 2174–2187. https://doi.org/10.1016/j.ultrasmedbio.2019.03.016

24. Thompson, R. F., Walker, M., Siebert, C. A., Muench, S. P., & Ranson, N. A. (2016). An introduction to sample preparation and imaging by cryo-electron microscopy for structural biology. *Methods (San Diego, Calif.)*, *100*, 3–15. https://doi.org/10.1016/j.ymeth.2016.02.017

25. de Leon, A., Perera, R., Hernandez, C., Cooley, M., Jung, O., Jeganathan, S., Abenojar, E., Fishbein, G., Sojahrood, A. J., Emerson, C. C., Stewart, P. L., Kolios, M. C., & Exner, A. A. (2019). Contrast enhanced ultrasound imaging by nature-inspired ultrastable echogenic nanobubbles. *Nanoscale*, *11*(33), 15647–15658. https://doi.org/10.1039/C9NR04828F

26. Streeter, I., Harrison, P. W., Faulconbridge, A., The HipSci Consortium, Flicek, P., Parkinson, H., & Clarke, L. (2017). The human-induced pluripotent stem cell initiative—Data resources for cellular genetics. *Nucleic Acids Research*, *45*(D1), D691–D697. https://doi.org/10.1093/nar/gkw928

27. Neal, E. H., Marinelli, N. A., Shi, Y., McClatchey, P. M., Balotin, K. M., Gullett, D. R., Hagerla, K. A., Bowman, A. B., Ess, K. C., Wikswo, J. P., & Lippmann, E. S. (2019). A Simplified, Fully Defined Differentiation Scheme for Producing Blood-Brain Barrier Endothelial Cells from Human iPSCs. *Stem Cell Reports*, *12*(6), 1380–1388. https://doi.org/10.1016/j.stemcr.2019.05.008

28. Yamashita, S., Konishi, K., Yamazaki, Y., Taki, Y., Sakane, T., Sezaki, H., & Furuyama, Y. (2002). New and better protocols for a short-term Caco-2 cell culture system. *Journal of Pharmaceutical Sciences*, *91*(3), 669–679. https://doi.org/10.1002/jps.10050

29. Lea, T. (2015). Caco-2 Cell Line. In K. Verhoeckx, P. Cotter, I. López-Expósito, C. Kleiveland, T. Lea, A. Mackie, T. Requena, D. Swiatecka, & H. Wichers (Eds.), *The Impact of Food Bioactives on Health* (pp. 103–111). Springer International Publishing. https://doi.org/10.1007/978-3-319-16104-4_10

30. Cucullo, L., Couraud, P.-O., Weksler, B., Romero, I.-A., Hossain, M., Rapp, E., & Janigro, D. (2008). Immortalized human brain endothelial cells and flow-based vascular modeling: A marriage of convenience for rational neurovascular studies. *Journal of Cerebral Blood Flow and Metabolism: Official Journal of the International Society of Cerebral Blood Flow and Metabolism*, *28*(2), 312–328. https://doi.org/10.1038/sj.jcbfm.9600525

31. DeStefano, J. G., Xu, Z. S., Williams, A. J., Yimam, N., & Searson, P. C. (2017). Effect of shear stress on iPSC-derived human brain microvascular endothelial cells (dhBMECs). *Fluids and Barriers of the CNS*, *14*(1), 20. https://doi.org/10.1186/s12987-017-0068-z

32. Helms, H. C., Abbott, N. J., Burek, M., Cecchelli, R., Couraud, P.-O., Deli, M. A., Förster, C., Galla, H. J., Romero, I. A., Shusta, E. V., Stebbins, M. J., Vandenhaute, E., Weksler, B., & Brodin, B. (2016). In vitro models of the blood-brain barrier: An overview of commonly used brain endothelial cell culture models and guidelines for their use. *Journal of Cerebral Blood Flow and Metabolism: Official Journal of the International Society of Cerebral Blood Flow and Metabolism*, *36*(5), 862–890. https://doi.org/10.1177/0271678X16630991

33. Deosarkar SP, Prabhakarpandian B, Wang B, Sheffield JB, Krynska B, et al. (2015) A Novel Dynamic Neonatal Blood-Brain Barrier on a Chip. PLOS ONE 10(11): e0142725. https://doi.org/10.1371/journal.pone.0142725

34. Lelu, S., Afadzi, M., Berg, S., Aslund, A. K., Torp, S. H., Sattler, W., & de L Davies, C. (2017). Primary Porcine Brain Endothelial Cells as In Vitro Model to Study Effects of Ultrasound and Microbubbles on Blood-Brain Barrier Function. *IEEE transactions on ultrasonics, ferroelectrics, and frequency control*, *64*(1), 281–290. https://doi.org/10.1109/TUFFC.2016.2597004

35. Blomley, M. J. K., Cooke, J. C., Unger, E. C., Monaghan, M. J., & Cosgrove, D. O. (2001). Microbubble contrast agents: A new era in ultrasound. *BMJ*, *322*(7296), 1222–1225. https://doi.org/10.1136/bmj.322.7296.1222

36. Miller MW. Gene transfection and drug delivery. *Ultrasound Med Biol.* 2000;26 Suppl 1:S59–S62. doi: 10.1016/S0301-5629(00)00166-6.

37. Tsutsui, J. M., Xie, F., & Porter, R. T. (2004). The use of microbubbles to target drug delivery. *Cardiovascular Ultrasound*, *2*, 23. https://doi.org/10.1186/1476-7120-2-23

38. Konofagou, E. E., Tung, Y.-S., Choi, J., Deffieux, T., Baseri, B., & Vlachos, F. (2012). Ultrasound-Induced Blood-Brain Barrier Opening. *Current Pharmaceutical Biotechnology*, *13*(7), 1332–1345.

39. Sun, T., Samiotaki, G., Wang, S., Acosta, C., Chen, C. C., & Konofagou, E. E. (2015). Acoustic cavitation-based monitoring of the reversibility and permeability of ultrasound-induced blood-brain barrier opening. *Physics in Medicine and Biology*, *60*(23), 9079–9094. https://doi.org/10.1088/0031-9155/60/23/9079

40. Attard, P. (2014). The stability of nanobubbles. *The European Physical Journal Special Topics*, *223*(5), 893–914. https://doi.org/10.1140/epjst/e2013-01817-0

41. de Leon, Al & Perera, Reshani & Hernandez, Christopher & Cooley, Michaela & Jung, Olive & Jaganathan, Selva & Abenojar, Eric & Fishbein, Grace & Sojahrood, Amin & Emerson, Corey & Stewart, Phoebe & Kolios, Michael & Exner, Agata. (2019). Contrast Enhanced Ultrasound Imaging by Nature-Inspired Ultrastable Echogenic Nanobubbles. Nanoscale. 11. 10.1039/C9NR04828F.

42. Batchelor, D. V. B., Armistead, F. J., Ingram, N., Peyman, S. A., Mclaughlan, J. R., Coletta, P. L., & Evans, S. D. (2021). Nanobubbles for therapeutic delivery: Production, stability and current prospects. *Current Opinion in Colloid & Interface Science*, *54*, 101456. https://doi.org/10.1016/j.cocis.2021.101456

43. Toepke, M. W., & Beebe, D. J. (2006). PDMS absorption of small molecules and consequences in microfluidic applications. *Lab on a Chip*, *6*(12), 1484–1486. https://doi.org/10.1039/b612140c

44. Dong, X. (2018). Current Strategies for Brain Drug Delivery. *Theranostics*, *8*(6), 1481–1493. https://doi.org/10.7150/thno.21254

45. Leskinen JJ, Hynynen K. STUDY OF FACTORS AFFECTING THE MAGNITUDE AND NATURE OF ULTRASOUND EXPOSURE WITH IN VITRO SET-UPS. Ultrasound in Medicine and Biology. 2012;38(5):777-94. doi: 10.1016/j.ultrasmedbio.2012.01.019. PubMed PMID: WOS:000302577900007.

46. Leenhardt R, Camus M, Mestas JL, Jeljeli M, Abou Ali E, Chouzenoux S, Bordacahar B, Nicco C, Batteux F,Lafon C, Prat F. Ultrasound-induced Cavitation enhances the efficacy of Chemotherapy in a 3D Model of Pancreatic Ductal Adenocarcinoma with its microenvironment. Scientific Reports. 2019;9:9. doi: 10.1038/s41598-019-55388-0. PubMed PMID: WOS:000503031800003.

47. Cafarelli A, Verbeni A, Poliziani A, Dario P, Menciassi A, Ricotti L. Tuning acoustic and mechanical propertiesof materials for ultrasound phantoms and smart substrates for cell cultures. Acta Biomaterialia. 2017;49:368-78. doi: 10.1016/j.actbio.2016.11.049. PubMed PMID: WOS:000394062100029.